An Intelligent Neural Network Controlled Atmospheric Pressure Spatial Atomic Layer Deposition System for Tunable Metal Oxide Thin Films

by

Manfred Kao

A thesis
presented to the University of Waterloo
in fulfillment of the
thesis requirement for the degree of
Master of Applied Science
in
Mechanical and Mechatronics Engineeering (Nanotechnology)

Waterloo, Ontario, Canada, 2018

© Manfred Kao 2018

Author's Declaration

I hereby declare that I am the sole author of this thesis. This is a true copy of the thesis, including any required final revisions, as accepted by my examiners.

I understand that my thesis may be made electronically available to the public.

Abstract

Atmospheric pressure spatial atomic layer deposition (AP-SALD) is a novel thin film fabrication technique to create conformal and pin-hole free films. The growth rate of AP-SALD is hundreds of times greater than conventional vacuum based methods which makes AP-SALD particularly attractive for large-scale roll-to-roll manufacturing. In this work, an AP-SALD system was built from scratch, in situ characterization tools were developed to monitor film properties during the growth of the film, an artificial neural network (ANN) was trained to model the AP-SALD system and an inverse neural network algorithm was implemented to generate recipes to produce films with defined properties.

A commercial controller was used to interface with all the sensors and actuators in the AP-SALD system. A time-optimal 5th order trajectory with a drift algorithm was implemented to oscillate the substrate stage back and forth, and a feedback control with feedforward and an anti-windup algorithm was used to maintain the temperature of the substrate during deposition. The position error of the stage was visually imperceptible after 1000 oscillations and the temperature settling time of the stage was around 10 minutes which was significantly less than the time required to set up the AP-SALD system. The AP-SALD system was able to repeatably deposit zinc oxide (ZnO) films with diethylzinc and water as precursors.

In situ electrical and optical tools were developed to measure the resistivity, film thickness and bandgap during the deposition. A printed circuit board (PCB) was designed to act as the electrodes and the substrate. A source/measure unit along with custom electronics measured the resistance of the films. The ZnO film grew on the PCB in island formations

before coalescing into a continuous film. The bulk resistivity of ZnO was found to be approximately 15 $\Omega \cdot cm$. Reflectance spectroscopy was used to measure the bandgap and thickness of the film during the deposition by fitting the spectrum to the Tauc-Lorentz model. A bandgap of 3.18 eV was found for ZnO films. The lowest growth rate achieved was 0.27 nm per ALD cycle indicating there is some mixing of the precursors.

A shallow feedforward ANN was trained to model the AP-SALD. The mean squared error (MSE) of the training set and test set was 0.9792 and 1.3287, respectively, indicating a good fit that can generalize well to new data. An inverse neural network algorithm was implemented to find the deposition parameters given the desired film properties. Since there may be infinite solutions, the algorithm returns the first optimal solution. The MSE of the estimated parameters were $2.5851 \cdot 10^{-14}$ indicating the algorithm was able to accurately inverse the AP-SALD model.

Acknowledgements

Foremost, I would first like to express my most profound gratitude to Dr. Kevin Musselman for the continuous support throughout my study and research. His door was always open whenever I needed guidance or advice about my research and whenever I wanted to chat.

Secondly, I would also like to thank Neil Griffett, the electronics technician, of the Mechanical and Mechatronics Engineering Department at the University of Waterloo. His expertise and assistance with anything electronics related in my research were unparallel.

Thirdly, I would like to recognize Kissan Mistry, a Ph.D. student at the University of Waterloo, for helping me complete a significant part of my research. Kissan along with Travis Yeow, a Master's student at the University of Waterloo, assisted in the optimization of the AP-SALD system.

Lastly, I must thank my friends and family for their unconditional love and support throughout my academic journey. I would not be in the position I am today if it weren't for them.

Table of Contents

List of Figures viii

List of Tables xi

1 Introduction 1

1.1 Atomic Layer Deposition and Applications 2

1.2 Atmospheric Pressure Spatial Atomic Layer Deposition 5

1.3 Artificial Neural Network 10

1.4 Thesis Overview 12

2 Construction of an AP-SALD 13

2.1 AP-SALD Control System Overview 16

2.2 Precursor Delivery System 18

2.3 Flow Control 20

2.4 Pneumatic Valves 23

2.5 Motor Trajectory 24

2.6 Heated Stage 27

3 In Situ Characterization Tools 32

3.1 In Situ Electrical Characterization 34

3.2 In Situ Optical Characterization 39

4 **Artificial Neural Network** **45**
4.1 Architecture 46
4.2 Training 47
4.3 Inverse Neural Network 50

5 **Conclusion** **54**
5.1 Future Work 56

References **58**

APPENDICES **67**

A **AP-SALD Construction** **68**
A.1 AP-SALD Human Machine Interface 69
A.2 Opto 22 Products 70
A.3 Flow Meters Details 71
A.4 Pneumatic Valves Details 72
A.5 Servo Drive Details 73
A.6 Motor Trajectory Details 74
A.7 Substrate Heater Details 78

B **In Situ Characterization Details** **80**

C **Artificial Neural Network Details** **91**

List of Figures

1.1 A digram illustrating one ALD cycle with DEZ as precusor A and H_2O as precursor B . . . 3

1.2 A diagram illustrating the difference between ALD and AP-SALD. (a) In conventional ALD, different precursor gases are exposed at different times. (b) In AP-SALD, different precursor gases are exposed at the same time but are separated in space. . . . 4

1.3 A simple diagram illustrating the production of precursor gases . . . 6

1.4 An illustration of a reactor head separating different precursor gases between curtains of inert gas . . . 7

1.5 An illustration of the exhaust channels in a reactor head . . . 8

1.6 144.6 nm thick ZnO film deposited with AP-SALD on borosilicate glass at 150°C using DEZ and H_2O as precursors . . . 9

2.1 Dr. Kevin Musselman's AP-SALD system at the University of Waterloo . . 14

2.2 The controller, brain, mounting rack and I/O modules used to implement the control system of the AP-SALD . . . 17

2.3 Bubblers used to hold the precursors and generate precursor gases in the AP-SALD . . . 19

2.4 Brooks 4850 (white) and Sierra Intruments' SmartTrak 50 Series (black) mass flow meters used to control the nitrogen flow in the AP-SALD system 21

2.5 5th order motion profile used to oscillate the subtrate during deposition . . 25

2.6 Resistive heating wire used to maintain the substrate at a certain temperature 28

2.7 The step response of the temperature controller of the heated stage 31

3.1 The AP-SALD system equipped with a reflectance probe and a high-temperature printed circuit board . . . 33
3.2 Custom flexible high-temperature PCB for in situ resistivity characterization 34
3.3 Circuit designed to route the SMU probes to the appropriate traces on the PCB . . . 35
3.4 Resistance plot (a) of a ZnO film across a high temperature flexible PCB (b). Each line in (a) corresponds to the resistance measured every third oscillations after the 15th oscillations. . . . 36
3.5 Resistance (a) and resistivity (b) in situ characterization of ZnO film on PCB. Each line corresponds to the resistance/resistivity measured every third oscillations after the 15th oscillations. . . . 38
3.6 Reflectance spectrum fitted with the Tauc-Lorentz model (a) to determine thickness and Tauc plot (b) to determine bandgap . . . 41
3.7 Film thickness as a function of the number of oscillation of the neural network training data obtained using the in situ optical measurement technique 43

4.1 A plot of an ANN fitting the in situ thickness measurement with 100 SCCM of precursor flow and 208 SCCM of nitrogen curtain flow . . . 48
4.2 A plot of an ANN fitting the in situ thickness measurement of all nine films at oscillation number 249 . . . 49
4.3 The regression plot (a) and the error histrogram (b) of the inverse neural network algorithm . . . 52

A.1 The human machine interface of the AP-SALD system . . . 69
A.2 Schematic diagram of the solenoid circuit . . . 72
A.3 Solenoid circuit used to control the pneumatic manifold . . . 72
A.4 Schematic diagram of the differential line driver used to convert the signals from the SNAP-SCM-ST2 to the servo drive . . . 73
A.5 Differential line driver used to send velocity commands to the servo drive . 73
A.6 Schematic of the resistive heating circuit to heat the stage during deposition 78
A.7 Photo of the resistive heating circuit to heat the stage during deposition . 78

A.8 Block diagram of the temperature controller used to set the temperature of the substrate in the AP-SALD system 79

B.1 Thickness as a function of number of oscillations deposited with 50 SCCM of precursor and 125 SCCM of nitrogen curtain 82
B.2 Thickness as a function of number of oscillations deposited with 100 SCCM of precursor and 125 SCCM of nitrogen curtain 83
B.3 Thickness as a function of number of oscillations deposited with 150 SCCM of precursor and 125 SCCM of nitrogen curtain 84
B.4 Thickness as a function of number of oscillations deposited with 50 SCCM of precursor and 208 SCCM of nitrogen curtain 85
B.5 Thickness as a function of number of oscillations deposited with 100 SCCM of precursor and 208 SCCM of nitrogen curtain 86
B.6 Thickness as a function of number of oscillations deposited with 150 SCCM of precursor and 208 SCCM of nitrogen curtain 87
B.7 Thickness as a function of number of oscillations deposited with 50 SCCM of precursor and 333 SCCM of nitrogen curtain 88
B.8 Thickness as a function of number of oscillations deposited with 100 SCCM of precursor and 333 SCCM of nitrogen curtain 89
B.9 Thickness as a function of number of oscillations deposited with 150 SCCM of precursor and 333 SCCM of nitrogen curtain 90

C.1 A plot of the ANN's performance as a function of epochs 91
C.2 The error histogram of the ANN where the x-axis is divided into 20 bins. The size of each bin is $\sim$0.67. The error of each data point is sorted into the corresponding bins. The closer the instances of error are around the zero error line, the better the fit. 92
C.3 The regression plot of the ANN where the x-axis is the target value the ANN is trying to predict. The y-axis is the true output of the ANN. A perfect fit will result in all data point on the Y=T line (slope of 1 and y-intercept of 0) and an R-value of 1. 93

List of Tables

3.1 Deposition parameters for in situ resistance measurements 37
3.2 Fixed deposition parameters during the collection of training data 42

A.1 Opto 22 I/O modules and their usage in the AP-SALD system 70
A.2 Flow meter operating ranges 71
A.3 Pinout for the flow meters and the Opto 22 I/O modules 71
A.4 Control parameters used in the substrate heater 79

Chapter 1

Introduction

1.1 Atomic Layer Deposition and Applications

Atomic Layer Deposition (ALD) is a well-studied technique used in nanotechnology to create conformal and pin-hole free films by sequentially exposing a substrate to self-limiting surface half-reactions [1]. The films are produced by saturating the surface of the sample with alternating precursor gases. Precursor gases are highly reactive gases or vapors that are usually created by bubbling an inert gas such as argon or nitrogen through a volatile liquid (see Figure 1.3). When the precursor is introduced to the sample, the molecules will adsorb and thoroughly saturate the surface of the sample. The next precursor will react with the molecules that were previously adsorbed to form a monolayer on the surface of the sample (Figure 1.1). This cycle is repeated until the desired film properties are achieved. The precursors used dictate the material of the film produced. For example, diethylzinc (DEZ) and water (H_2O) are commonly used precursors to create zinc oxide (ZnO) films. A simplified reaction mechanism is shown in Equation 1.1. For a more in-depth explanation of the reaction between DEZ and H_2O see [2]. The sample is heated to induce the reaction of the precursor gases to occur only on the surface of the sample. A purge step is required between each exposure of different precursor gases to evacuate any excess molecules that have not been adsorbed onto the surface of the sample to prevent the precursors from reacting in the gas phase (see Figure 1.2(a)). One ALD cycle (shown in Figure 1.1), defined as Precursor A → Purge → Precursor B → Purge, produces a single monolayer on the surface of the sample.

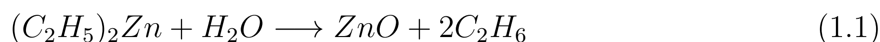

$$(C_2H_5)_2Zn + H_2O \longrightarrow ZnO + 2C_2H_6 \tag{1.1}$$

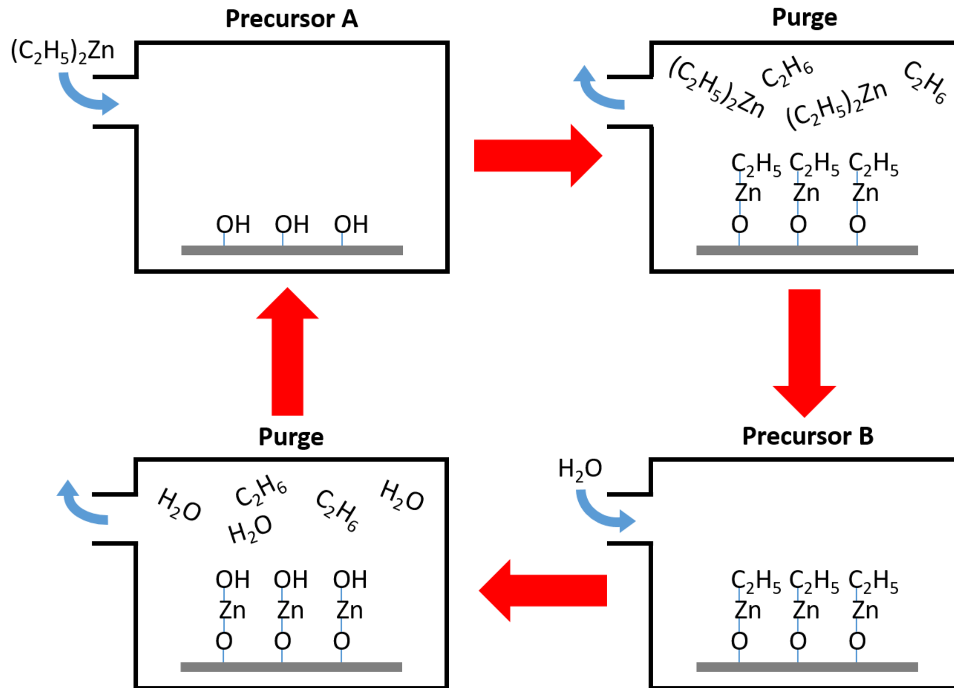

Figure 1.1: A digram illustrating one ALD cycle with DEZ as precusor A and H_2O as precursor B

ALD has been proven to be a powerful tool in many applications. In [3], ALD was used to produce high-k dielectric and metal films for metal-oxide-semiconductor field-effect-transistors, create dynamic random-access memory capacitors and fabricate thin film magnetic heads. In [4], Carcia *et al.* used ALD to produce a thin Al_2O_3 film as a moisture barrier to reduce the water vapor transmission rate for organic light emitting diodes. Meng *et al.* designed new lithium-ion components such as anode, cathode, and inorganic electrodes with ALD to modify the battery properties [5]. ALD was also shown to have many applications in solid oxide fuel cell research as discussed in [6]. Finally, ALD can be used

for photovoltaics as shown in [7] and [8].

Although ALD has been proven to be a powerful tool with many applications in a broad range of industries, it has its drawbacks. Namely, the low deposition rate (hundredths of nanometer per second [9]) due to the long purge step and the need for a vacuum chamber render this technology incompatible for large-scale high-throughput roll-to-roll manufacturing [10].

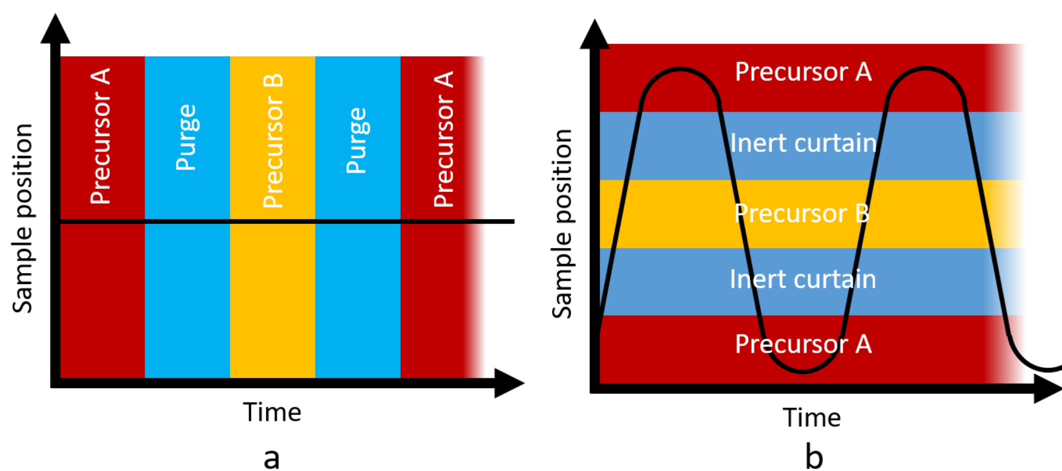

Figure 1.2: A diagram illustrating the difference between ALD and AP-SALD. (a) In conventional ALD, different precursor gases are exposed at different times. (b) In AP-SALD, different precursor gases are exposed at the same time but are separated in space.

1.2 Atmospheric Pressure Spatial Atomic Layer Deposition

Atmospheric Pressure Spatial Atomic Layer Deposition (AP-SALD) is a novel technique that relies on similar mechanisms as ALD to produce thin films but eliminates the issues mentioned above. Rather than exposing the sample to precursor gases sequentially, thus, separating them in time, AP-SALD exposes the sample to all the precursors at the same time but physically separates them in space (Figure 1.2(b)) [10]. Similar to ALD, the precursor gases are produced by bubbling an inert gas through a volatile liquid to pick up a small amount of precursor vapor. This vapor is then combined with an inert carrier line which is then supplied to a specially design reactor head (See Figure 1.3 for a diagram). The flow rate of the bubbler line and carrier line is usually controlled by a mass flow controller (MFC). The purpose of the carrier line is to dilute the precursor vapors from the bubblers.

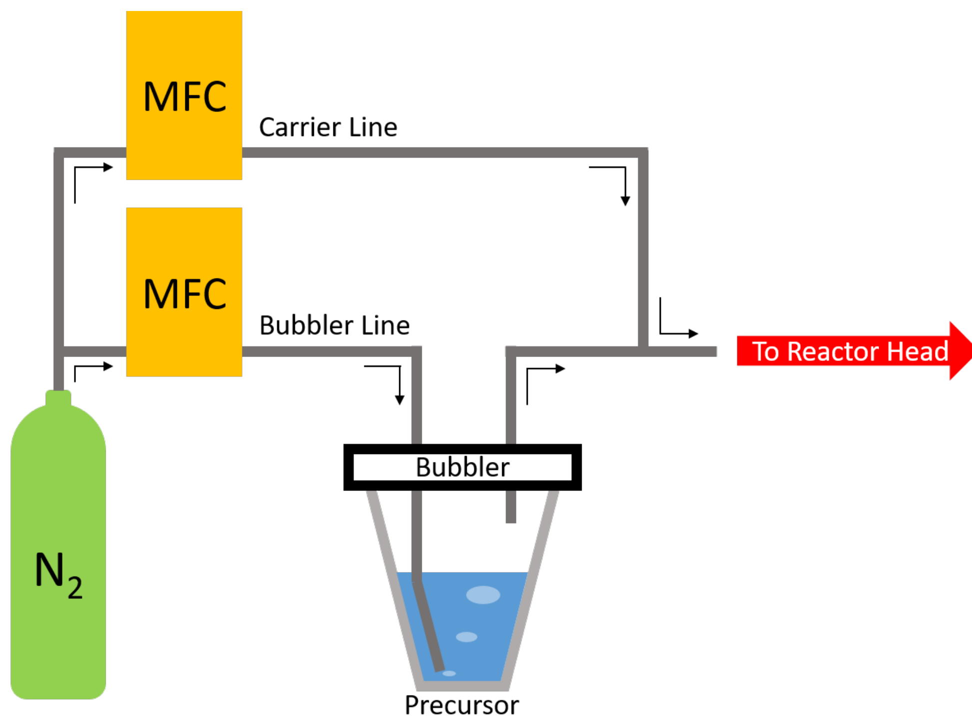

Figure 1.3: A simple diagram illustrating the production of precursor gases

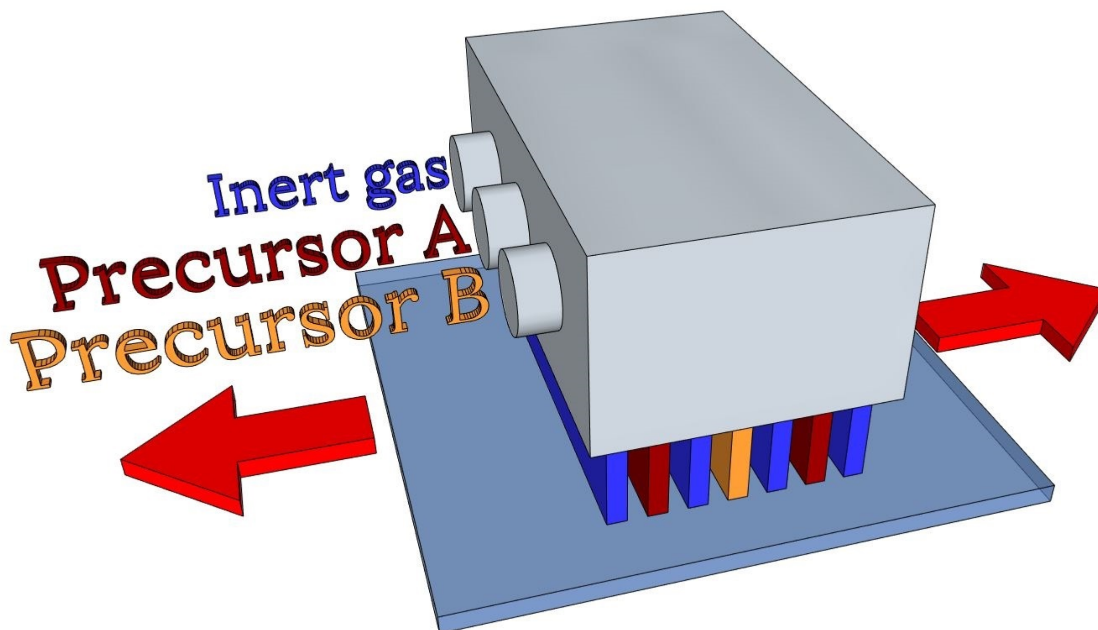

Figure 1.4: An illustration of a reactor head separating different precursor gases between curtains of inert gas

The reactor head is used to separate the continuously flowing precursor gases by introducing a curtain of inert gas between the precursor gases. The curtain of inert gas prevents the different precursor gases from mixing in air and by extension, ensures the reactions to only occur on the surface of the sample. A simple illustration of a reactor head is shown in Figure 1.4. If there is insufficient separation of the precursor gases and the reaction occurs in the gas phase before depositing onto the sample, chemical vapor deposition (CVD) will be achieved. The exhaust channels in the reactor head are situated between every pairs of gas channels (precursor and inert curtain) to remove excess gas that did not adsorb onto

the surface of the sample (see Figure 1.5). For this reason, the AP-SALD system does not need to be in a vacuum chamber to evacuate the excess gases, and as a result, a film can be produced in atmospheric conditions.

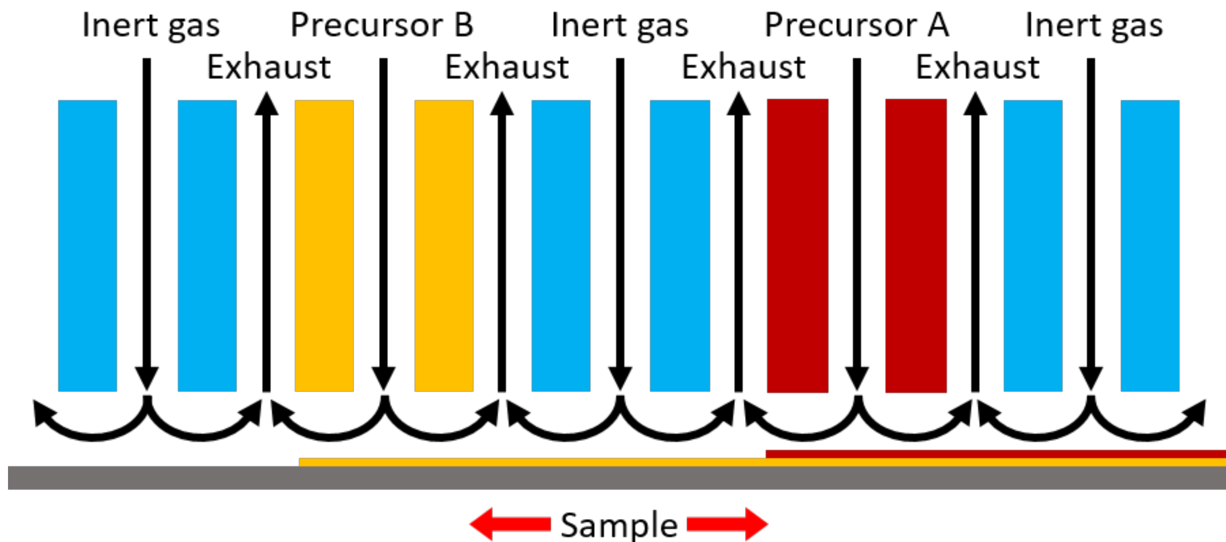

Figure 1.5: An illustration of the exhaust channels in a reactor head

The sample oscillates back and forth underneath the reactor head to ensure every part of the sample is exposed to all the different precursor gases. Since the reactor head can be lengthened to accommodate as many precursor channels as desired, one pass under the reactor head can be equivalent to multiple ALD cycles making AP-SALD far superior to ALD in regards to scalability. An image of a 144.6 nm thick ZnO film deposited with AP-SALD on borosilicate glass is shown in Figure 1.6.

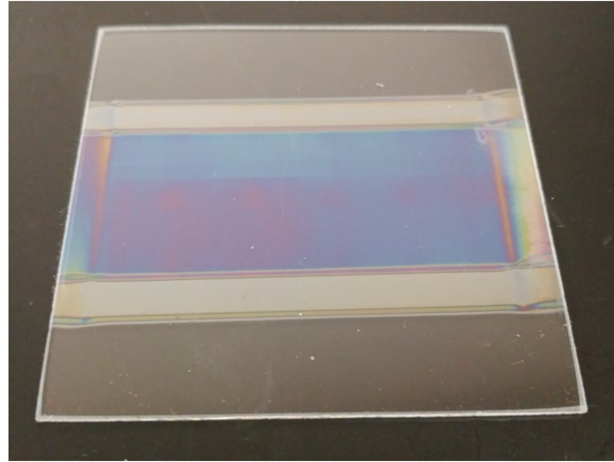

Figure 1.6: 144.6 nm thick ZnO film deposited with AP-SALD on borosilicate glass at 150°C using DEZ and H_2O as precursors

1.3 Artificial Neural Network

With the advent of computational material databases and related data-driven material discovery approaches developed in the past five years, more than 20 new functional materials for various applications have been identified and confirmed by experiments [11]. For instance, high-throughput computational screening studies have discovered new metal oxide perovskites and oxynitrides materials for photocatalysis applications [12–14]. It is often difficult for humans to make sense of large datasets. However, machine learning algorithms are capable of performing this task with relative ease. Machine learning has been used to discover new materials from failed attempts with an 89% success rate [15] and to determine critical parameters controlling the spin-Seebeck effect which led to the identification of a new material with performance an order of magnitude greater than the current technology [16].

To optimize the performance of devices such as solar cells, thin-film transistors, and transparent conducting oxides, precise control of the film properties is required [17–22]. By varying the AP-SALD deposition parameters such as deposition temperature, exposure time, precursor partial pressure and dopant concentrations, the capability of tuning the properties of ZnO films has been demonstrate [17, 19, 20, 22, 23]. Although in situ characterization of thin films produced with ALD and AP-SALD have been studied in the past [24–30], this information has not been used to develop a controller to generate recipes for tunable thin films by mapping film properties to deposition parameters.

In recent years, artificial neural networks (ANNs) have been shown to be a powerful tool in seemingly unrelated applications ranging from power electronics and motor drives [31],

geotechnical engineering [32], medical imaging and signal processing [33], finance [34], and sleep research [35]. Although ANNs have been used to model and optimize the growth rates of thin films [36, 37], ANNs have not been applied to thin films produced by AP-SALD. ANNs are mathematical models that can approximate any Borel measurable function to any degree of accuracy, given there are enough hidden neurons in the network [38]. Such mathematical models are known as universal approximators. In this work, an ANN was used to model the AP-SALD system which was then used to develop an inverse neural network algorithm to provide recipes to produce thin films with any achievable properties. The ANN will be an excellent tool for new material discovery, precise film property control and high throughput screening of new materials.

1.4 Thesis Overview

In this paper, the construction of an AP-SALD system will be discussed in detail in Chapter 2, the development of in situ characterization tools will be outlined in Chapter 3 and lastly, the implementation of an ANN for film property control will be disclosed in Chapter 4.

Chapter 2

Construction of an AP-SALD

An AP-SALD system was built from scratch at the University of Waterloo in Dr. Kevin Musselman's lab. Dr. Kevin Musselman's AP-SALD system was based on the design of Dr. David Muñoz-Rojas's AP-SALD system at the Laboratory in Materials Science and Physical Engineering in Grenoble, France. The AP-SALD, shown in Figure 2.1, was entirely designed and built by co-op and graduate students from the University of Waterloo.

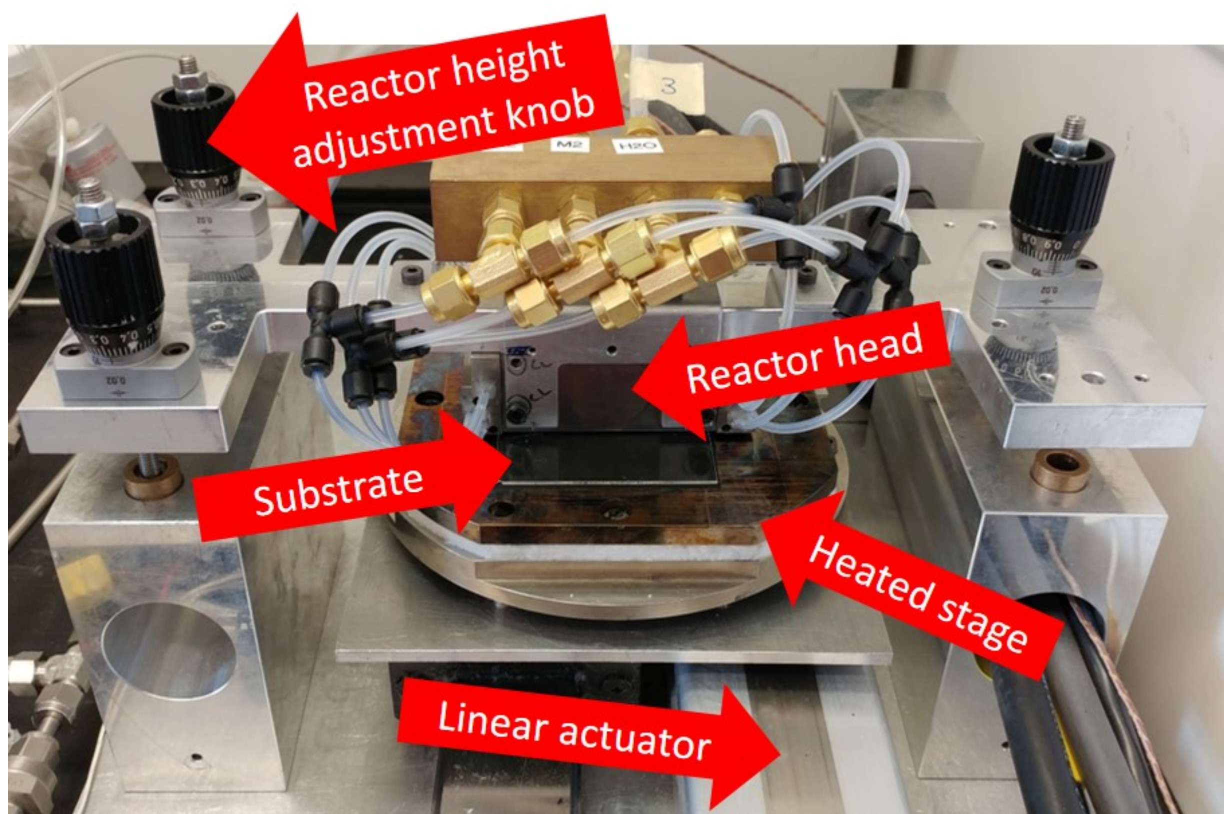

Figure 2.1: Dr. Kevin Musselman's AP-SALD system at the University of Waterloo

Stella Kim (co-op student) modeled the preliminary design of the AP-SALD system in computer-aided design software. Ashley Liu (co-op student) modeled and fabricated the first version of the reactor assembly and the stage that holds the sample. Rohan Agarwal (co-op student) designed the precursor delivery system, fabricated the stand that held the precursor bubblers and acquired some of the control system components. My contributions to the development of the AP-SALD system included the design and fabrication of all

the electronics, the software and the human machine interface (HMI). Francis Uzoma (MASc student), Scott Smith (co-op student), Jasdeep Dhillon (co-op student) and Reid Wotton (co-op student) were responsible for the physical components of the AP-SALD such as machining various parts, routing the inert and precursor lines, redesigning the stand that holds the reactor head, etc. Kissan Mistry (Ph.D. student) and Travis Yeow (MASc student) aided in debugging and optimization of the AP-SALD system.

2.1 AP-SALD Control System Overview

A commercial controller with input/output (I/O) modules to communicate with the various system components was used to develop the control system of the AP-SALD. The brain, controller, and I/O modules were all purchased from Opto 22. All the software for the AP-SALD system was written in PAC Control Basic, and the Human Machine Interface was developed on PAC Display Basic. The part number of the Opto 22 products along with a short description are summarized in Table A.1 in Appendix A, Section A.2.

The SNAP-PAC-R1 comprises of a controller and a brain, whereas, the SNAP-PAC-EB1 is just a brain. The role of a controller is to process the algorithms written in PAC Control Basic and to communicate with the brains. The brain receives requests from the controller to send and transmit data to and from the I/O modules. The brain interfaces with the I/O modules via a SNAP-PAC-RCK16 mounting rack. The AP-SALD system utilizes two brains and two mounting racks to accommodate all the I/O modules used. Figure 2.2 shows all the Opto 22 products used in the AP-SALD.

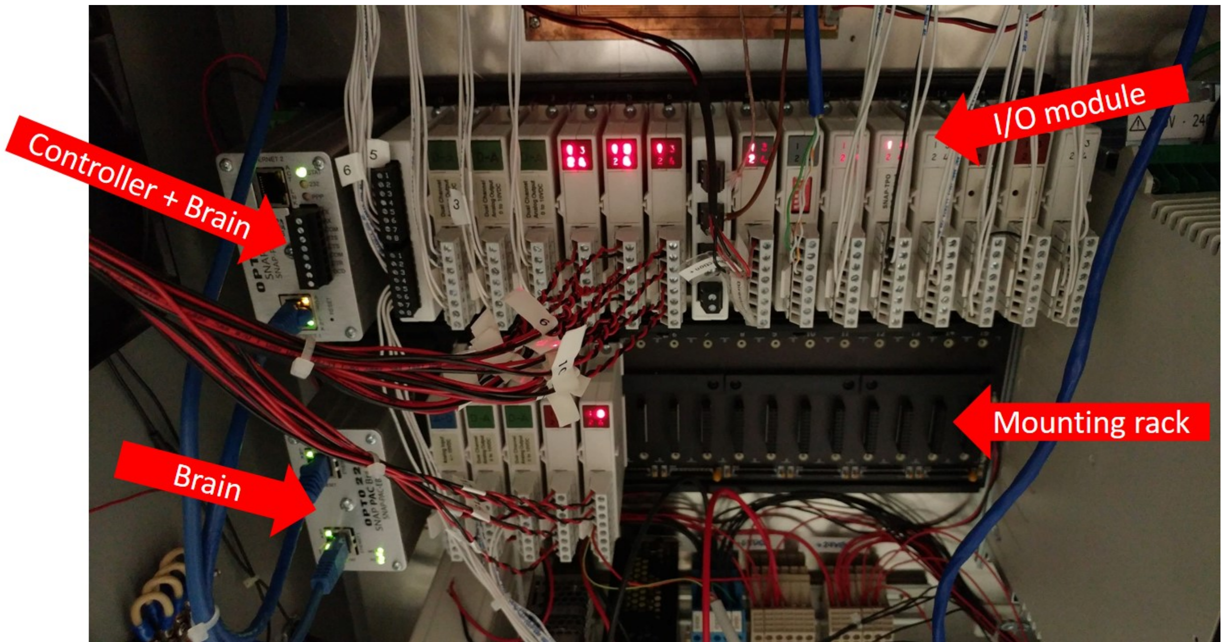

Figure 2.2: The controller, brain, mounting rack and I/O modules used to implement the control system of the AP-SALD

2.2 Precursor Delivery System

The precursors are held in the custom handmade glass vials (shown in Figure 2.3). Nitrogen gas was used to bubble the precursors contained in the vials to create vapors. The AP-SALD was designed to accommodate five different precursor gases; however, in this work, only two will be used. The precursor gases used are diethyl zinc (DEZ) and distilled water (H_2O) to create zinc oxide (ZnO) thin films. Nitrogen was also used as the gas for the carrier lines and the inert gas curtains. The reactor head is a stainless steel machined piece with two H_2O, one DEZ channel and six nitrogen curtain channels. One oscillation in the AP-SALD system is defined as passing the substrate underneath and back out of the reactor head, thus, making one AP-SALD oscillation equivalent to two ALD cycles. All the nitrogen used in the AP-SALD was supplied from a singled compressed nitrogen tank regulated to ~25 PSI.

Figure 2.3: Bubblers used to hold the precursors and generate precursor gases in the AP-SALD

2.3 Flow Control

All the flows in the system (bubbler, carrier, and curtain) were controlled electronically by Brooks 4850 and Sierra Instruments' SmartTrak 50 Series MFCs (shown in Figure 2.4). The MFCs are calibrated for nitrogen to operate within the flow rates that are summarized in Table A.2 in Appendix A, Section A.3. All MFCs use an analog voltage (0 - 5VDC) signal as their setpoint to set the flow rate. An Opto 22 Module is used to provide the analog voltage signal. A linear interpolation is used to map the desired flow rate to the corresponding input voltage. The built-in controllers in the Brooks and Sierra MFCs were used to track the defined flow rate. The pinout for the flow meters and the Opto 22 Module are detailed in Table A.3 in Appendix A, Section A.3.

Figure 2.4: Brooks 4850 (white) and Sierra Intruments' SmartTrak 50 Series (black) mass flow meters used to control the nitrogen flow in the AP-SALD system

The Brooks MFCs needed a warmup time of 15 minutes to control the flow rate accurately. A timer was implemented in software to allow the deposition to begin only after 15 minutes have passed. The Sierra MFCs will overheat when the flow is zero, but the setpoint is a non-

zero value for a prolonged period which occurs when the setpoint is non-zero, and either the valves are closed, or there is a blockage in the line. An algorithm was implemented to set the setpoint to zero when the flow rate drops below 80% of the setpoint for 10 seconds and to recover the original setpoint when the corresponding pneumatic valves are open.

2.4 Pneumatic Valves

There are numerous pneumatic valves in the AP-SALD system that are used to either turn on or off the gases to the reactor head or to switch the lines to have a different precursor gas flow to the reactor head. Switching the lines to a different precursor gas can be used to create films with dopants by simply mixing the different precursor gases in the lines before depositing onto the substrate or switch to a different precursor gas between layers. The pneumatic valves operate with compressed air that was supplied with an air compressor set to ∼80 PSI. A pneumatic manifold with a set of SMC V110-D5CU-C4 solenoid valves and a diode and fuse circuit were used to distribute the compressed air to the corresponding pneumatic valves. The diode and fuse circuit consisted of commutating diodes and fuses to prevent flyback from the solenoid coil and overcurrent from potentially damaging the digital output module. Figure A.2 and Figure A.3 in Appendix A in Section A.4 shows a detail schematic diagram of the solenoid valve and diode circuit.

2.5 Motor Trajectory

A Control Techniques XVM-403-TONS-0000 servo motor and THK VLAST60-06-0300-0-0N linear actuator were used to oscillate the substrate under the reactor head. The motor is driven by an Emerson Industrial Automation Digitax ST-B servo drive with an SM-Universal Encoder Plus module to read the encoder. The SNAP-SCM-ST2 Opto 22 module was used to command the angular velocity of the motor and the SNAP-SCM-485-422 Opto 22 module was used to read important feedback signals such as the motor position from the drive. The motor drive expects a differential signal for the velocity command. A custom circuit shown in Figure A.4 and Figure A.5 in Appendix A, Section A.5 was built to convert the signals.

The motion trajectory of the substrate is a smooth, time-optimal s-curve motion profile with 5th order model found in [39]. It has been shown that an s-curve motion profile with higher order models produces fewer vibrations in the high-frequency range [40]. Fewer high-frequency vibrations are desirable since the natural resonant frequency of the system is in the high-frequency range due to the rigidity of the structure. In [41], Nguyen *et al.* demonstrated the position error was significantly greater with lower order models when a linear motor was used to track the trajectories. A plot of the motion trajectory showing the jerk, $j(t)$, acceleration, $a(t)$, velocity, $v(t)$, and position, $x(t)$, is presented in Figure 2.5. The corresponding equations are shown in Equation A.1 to A.4 in Appendix A, Section 2.5.

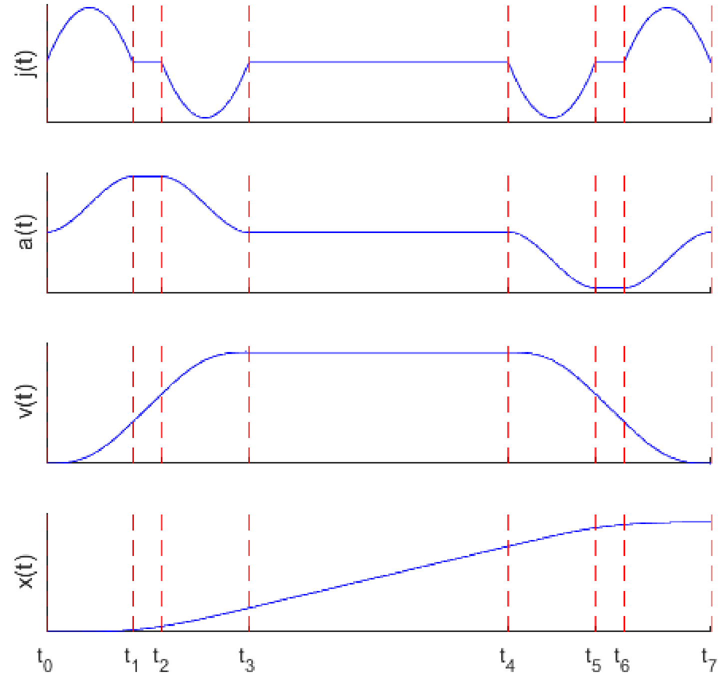

Figure 2.5: 5th order motion profile used to oscillate the subtrate during deposition

The trajectory was tuned to exhibit the greatest magnitude of jerk and acceleration while staying within the tolerances of the motor and linear actuator assembly to allow the substrate to reach the desired speed as quickly as possible to maximize the constant velocity region. A constant velocity region was needed to ensure the exposure time of precursor gases were constant across the surface of the sample which will result in a uniform deposition. Maximizing the constant velocity region will allow for the largest area of uniform deposition.

A small amount of drift was observed during a large number of oscillations. The position

error accumulates due to the servo drive controlling the velocity of the motor. A drift algorithm was developed to correct the drift. The encoder data was captured at the end of each trajectory and the time in the constant velocity region, T_4, was adjusted for the next trajectory to compensate for the error in the position. It was determined experimentally that the servo was not fast enough to simultaneously read the encoder and send a velocity command. Therefore the error can only be corrected for the next trajectory. The drift algorithm was proven to be successful considering after 1000 oscillations, the position error at the start/end of the trajectories were determined visually to be negligible.

2.6 Heated Stage

The substrate needs to be heated to a certain temperature to promote the reaction of the precursor gases on the surface of the sample. During the deposition, the substrate is held on top of a nickel-plated copper stage by a vacuum pump. The stage was chosen to be made in copper due to its high thermal conductivity and plated in nickel to prevent oxidation. The stage is heated by a resistance heating wire that has a resistance of 3.5Ω and is rated for $700W$ (See Figure 2.6). A transformer is used to step down mains voltage to 48VAC to power the heating wire. A solid state relay was used to control the power to the heating wire via a pulse width modulation (PWM) signal generated by the SNAP-AOD-29 Opto 22 module. The SNAP-AOD-29 module generates a square wave with a variable duty cycle. A duty cycle is the fraction of a period where the signal is high, and it is usually expressed as a percentage from 0 to 100% [42]. The frequency of the PWM signal was set to $\sim$4Hz which was determined experimentally to be fast enough as no temperature fluctuations were recorded. A photo and schematic of the resistive heating circuit can be found in Figure A.6 and A.7, respectively, in Appendix A, Section A.7.

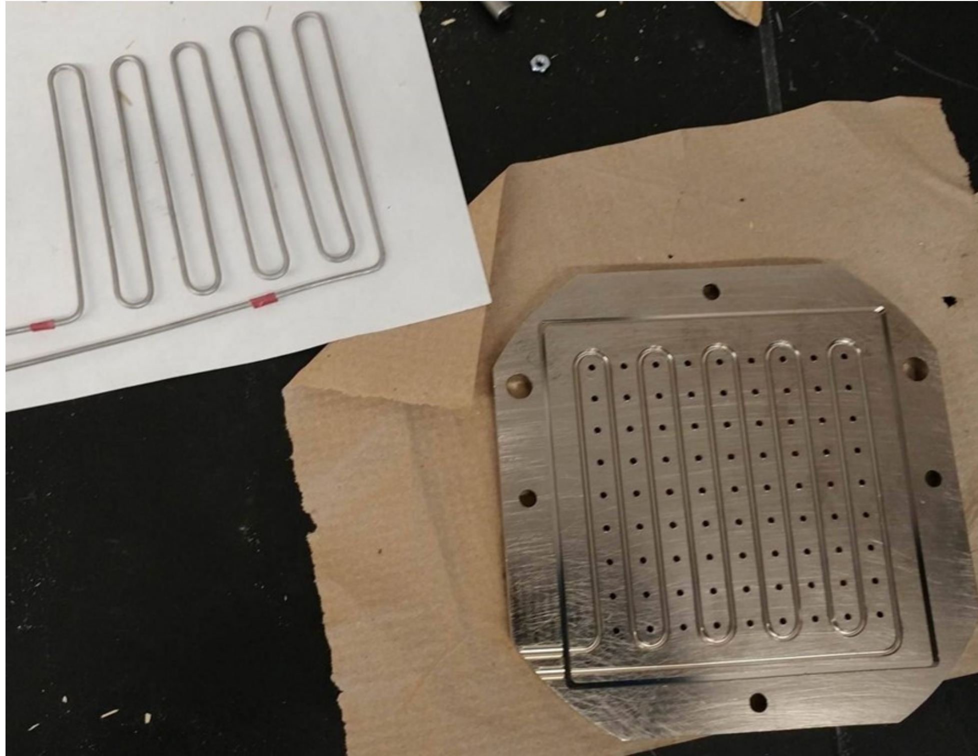

Figure 2.6: Resistive heating wire used to maintain the substrate at a certain temperature

The controller used to track the defined temperature is a proportional (P) and proportional-integral (PI) controller. The derivative of the error was not used because it was found through experimentation that the noise in the system caused the controller output to saturate. A thermocouple was used to provide temperature feedback to the controller. The controller gains were tuned using the Cohen-Coon method which can be found in Table A.4 in Appendix A, Section A.7. The Cohen-Coon tuning method was used because it does not require a mathematical model of the system. Instead, the parameters were tuned by analyzing the response of the system to a step change [43].

The anti-windup algorithm discussed in [44] was implemented to prevent integrator windup. The integral windup phenomena often occur when the output of the controller is constrained between an upper bound and a lower bound. In this case, the duty cycle of the PWM signal is constrained between 0 and 100%. When there is a large temperature error due to rapidly changing the desired temperature setpoint or effects of external disturbances, the controller output will likely saturate (to either 0 or 100%). The integral adjustment will continue to accumulate error despite the controller output being bounded which will lead to a large overshoot. For example, if the stage is at room temperature and the temperature setpoint was changed to 200°C, the integral adjustment will accumulate a large value before the stage reaches the desired 200°C. Once the temperature reaches 200°C, the integral adjustment will still be large and will inevitably cause an overshoot in temperature. To eliminate this issue, the anti-windup algorithm switches the controller between P and PI control. The pseudocode for the anti-windup algorithm is shown in Algorithm A.1 in Appendix A, Section A.7.

A simple feedforward control algorithm was implemented along with the feedback controller for a quicker convergence to steady state. The steady state temperature as a function of the PWM duty cycle, $f(\cdot)$, was determined experimentally. The inverse of the function, $f^{-1}(\cdot)$, was summed with the controller output as shown in Equation 2.1 below and Figure A.8 in Appendix A, Section A.7. The feedforward algorithm eliminated the time required for the integral adjustment to converge the appropriate PWM duty cycle for the corresponding steady state temperature.

$$PWM = K_c\left(e(t) + \frac{1}{T_i}\int e(t)dt\right) + f^{-1}(T_d) \tag{2.1}$$

Where K_c is the controller gain, T_i integral time, $e(t)$ is the temperature error, and T_d is the desired temperature setpoint.

Figure 2.7 shows the temperature setpoint, the temperature feedback and the controller output of the heated stage in the AP-SALD system. The controller can be seen switching from PI control to P control at the 88th and 433rd second to prevent integrator windup. The settling time of the system is defined as the time required for the error, $e(t)$, to reach and stay within 2% of the final value [45]. In Figure 2.7, the settling time is just over 10 minutes which is less than the 15 minutes required for the MFCs to warm up. The performance of the controller was proven to be sufficient for this application since high-performance temperature tracking is not needed.

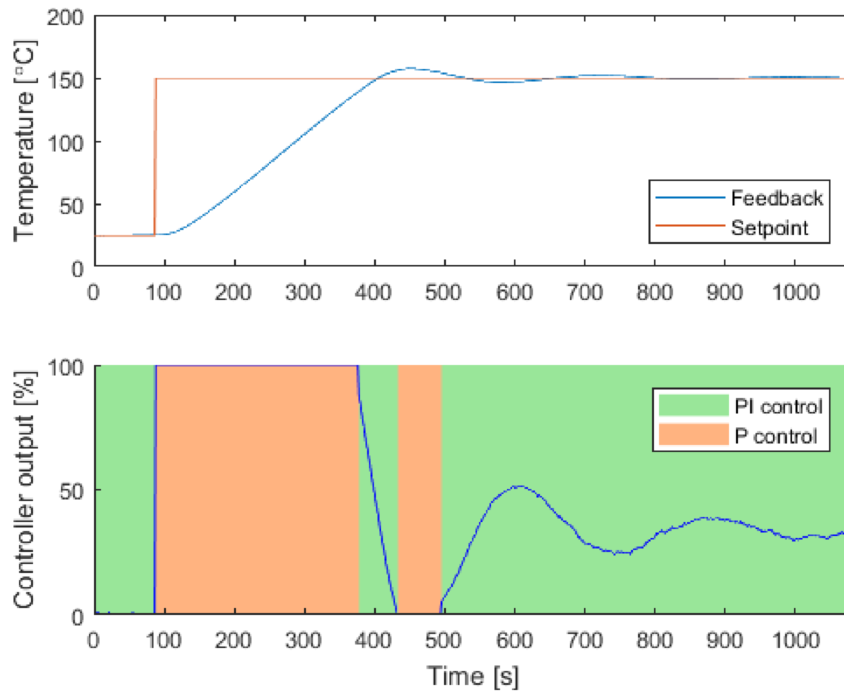

Figure 2.7: The step response of the temperature controller of the heated stage

Chapter 3

In Situ Characterization Tools

In Chapter 4, an improvement to the AP-SALD system involving the introduction of self-learning capabilities and property control with an ANN will be discussed. To train the ANN, training data was gathered with in situ electrical and optical characterization tools, shown in Figure 3.1, that measure the film properties during the growth of the film. Visual Basic was used to interface between PAC Control and the in situ characterization equipment, and MATLAB was used for all the in situ data processing.

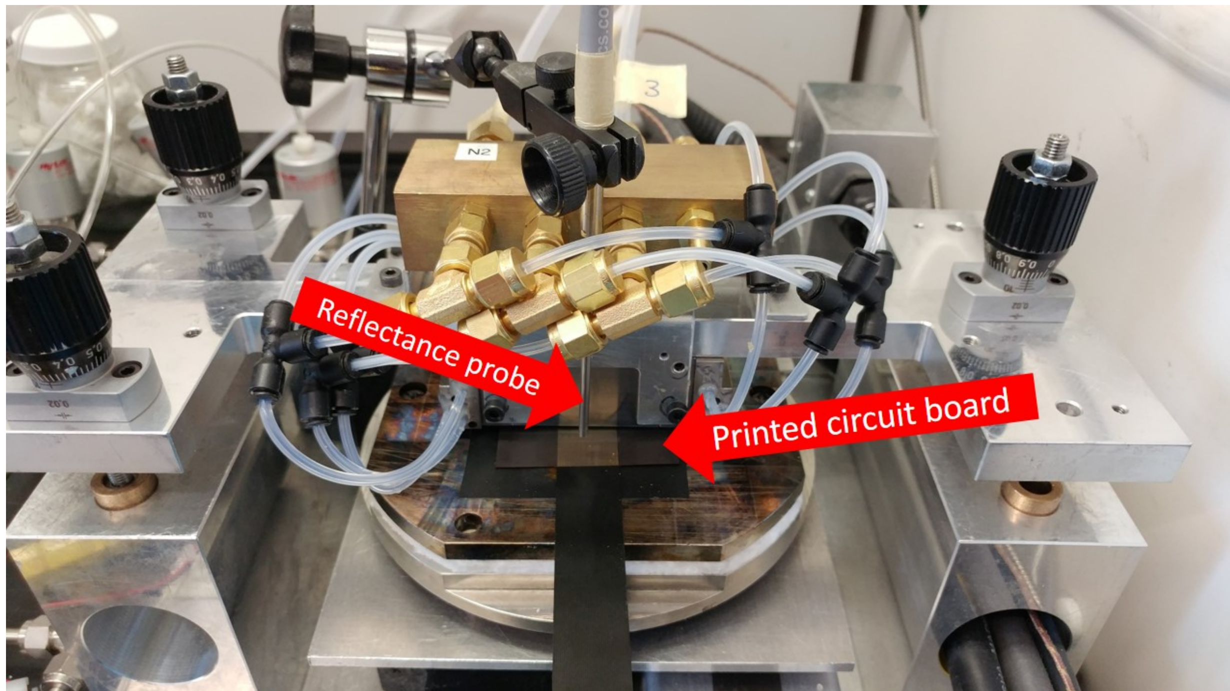

Figure 3.1: The AP-SALD system equipped with a reflectance probe and a high-temperature printed circuit board

3.1 In Situ Electrical Characterization

The resistance of the film was measured using a Keysight B2901A source/measure unit (SMU). A custom flexible high-temperature printed circuit board (PCB) with 40 copper traces, shown in Figure 3.2, was designed to act as the substrate and electrodes for in situ electrical characterizations. The film can be deposited right onto the PCB while the SMU measures the resistance during the growth of the film. The 20 pairs of electrodes allow for 20 measurements across the film which can be used to check uniformity or be used to characterize gradient films.

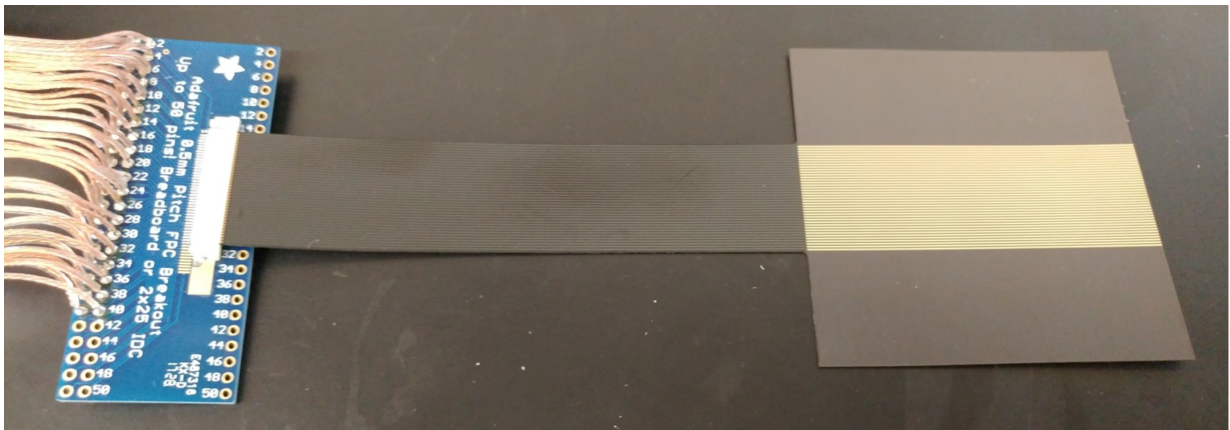

Figure 3.2: Custom flexible high-temperature PCB for in situ resistivity characterization

A circuit, shown in Figure 3.3, was designed to route the two probes from the SMU to the appropriate electrode pairs. The circuit consisted of 20 relays to route the SMU probes and an Arduino microcontroller to act as the brain of the circuit. To reduce the number of signal wires, the Arduino used a lookup table to decode the 6-bit digital signal sent from

two SNAP-ODC5SNK Opto 22 modules to energize the appropriate relays.

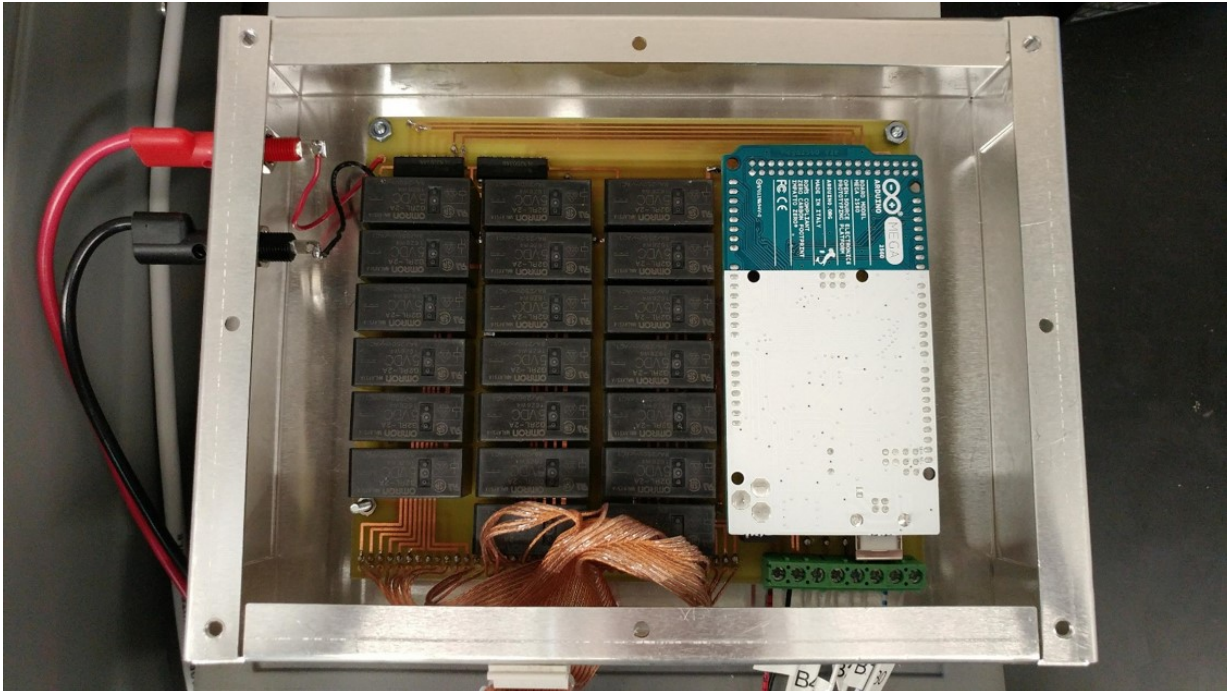

Figure 3.3: Circuit designed to route the SMU probes to the appropriate traces on the PCB

The resistivity of the film was calculated from

$$\rho = R\frac{lt}{w} \tag{3.1}$$

Where R is the measured resistance, l is the length of the traces, t is the thickness of the film, and w is the spacing between the traces. The thickness was determined by the optical characterization discussed in Section 3.2.

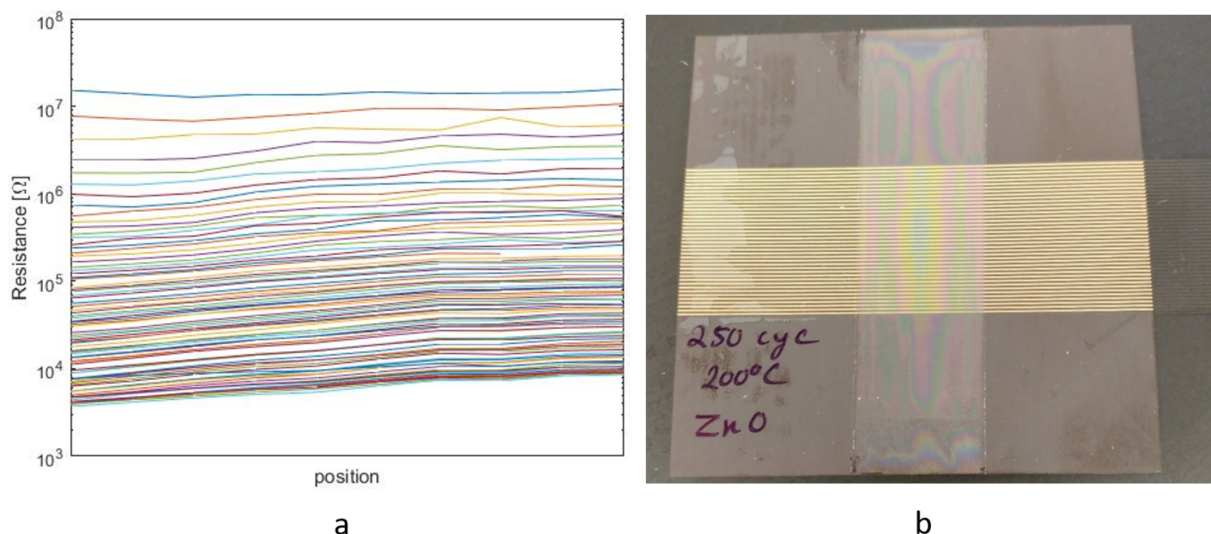

Figure 3.4: Resistance plot (a) of a ZnO film across a high temperature flexible PCB (b). Each line in (a) corresponds to the resistance measured every third oscillations after the 15th oscillations.

Figure 3.4(a) shows the resistance at various positions along a ZnO film that was deposited using the depositions parameters listed in Table 3.1. The traces were positioned parallel to the motion of the substrate. The SMU sourced a constant current of 20 mA and measured the voltage drop to calculate the resistance during the deposition. Each line corresponds to the resistance at a different number of oscillations starting at the 15th oscillation. Before 15 oscillations, the SMU was not sensitive enough to measure the high resistances. By visually inspecting the color of the film shown in Figure 3.4(b) and by examining the flatness of Figure 3.4(a), it is clear the film was not uniform. The non-uniformity can be attributed to the PCB expanding when heated causing it to warp and preventing it from laying flat

on the stage during deposition and the height difference between the Kapton tape and the PCB disturbing the flows under the reactor head. Kapton tape was used to mask off the region where the motor speed was not constant (left and right portions of Figure 3.4(b)).

Table 3.1: Deposition parameters for in situ resistance measurements

Deposition parameter	**Value**
H_2O bubbler flow rate	45 SCCM
H_2O carrier flow rate	255 SCCM
DEZ bubbler flow rate	23 SCCM
DEZ carrier flow rate	127 SCCM
Nitrogen curtain flow rate	900 SCCM
Oscillation speed	15 mm/s
Number of oscilations	250
Deposition Temperature	200°C
Reactor head height	100 μm

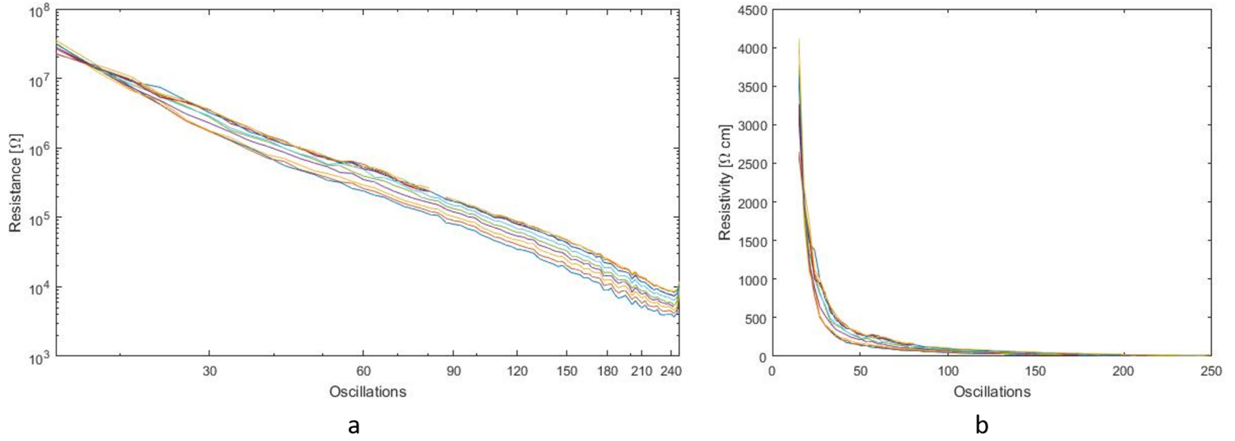

Figure 3.5: Resistance (a) and resistivity (b) in situ characterization of ZnO film on PCB. Each line corresponds to the resistance/resistivity measured every third oscillations after the 15th oscillations.

Figure 3.5(a) and (b) shows the resistance and resistivity of the ZnO film, respectively, as the film was deposited. Each line represents the resistance/resistivity between a different pair of traces on the PCB. The asymptotic behavior of the resistivity suggests that the ZnO deposited on the flexible PCB material grows in discontinuous islands at first which later coalesces into an electrically connected film [46]. The resistivity tends to $\sim 15\ \Omega \cdot cm$ as the film thickness increases. Although the resistivity was higher than what was reported in literature [47,48], it has been shown that the resistivity of thin films is heavily dependent on the deposition parameters and its thickness [23], which can explain the disparity.

3.2 In Situ Optical Characterization

An OceanHDX spectrometer and a DH-2000 light source from Ocean Optics were used to measure the thickness and bandgap of the film in situ, based on the reflectance spectrum. The intensity of the spectrum varies depending on the height of the reflectance probe and the reflectivity of the material being measured. The spectrum will saturate if the intensity is too high and vital features in the reflectance curve will be lost if the intensity is too low. The integration time is the length of time the detector captures light. Thus, changing the integration time will change the intensity of the reflectance plot. Ocean Optics engineers recommend setting the integration time so that the maximum intensity of the spectrum is between 80% to 90% of the saturation limit. An exponential search was used to find the appropriate integration time. More details including a pseudocode of the exponential search can be found in Algorithm B.1 in Appendix B.

After setting the appropriate integration time, the spectrometer needs to be calibrated to produce useful reflectance plots. A reference spectrum, R_{ref}, and a dark spectrum, R_{dark}, need to be captured to eliminate the effects of the light source and the spectrometer noise on the reflectance plot, respectively. The reference spectrum was captured by taking a reflectance measurement of a silicon wafer. Although the reflectance of a silicon wafer is not 100% reflective [49], it is more reflective than the ZnO films being produced. Thus, a silicon wafer is suitable for capturing the reference spectrum for this application. The dark spectrum was captured by simply closing the shutter and taking a measurement. The spectrum calibration equation is given by

$$R_{cal} = R_{cor} \frac{R_{raw} - R_{dark}}{R_{ref} - R_{dark}} \tag{3.2}$$

Where R_{raw} is the raw data from the spectrometer and R_{cor} is the correction factor. A correction factor is needed to adjust the intensity of the measured spectrum to match the simulated spectrum due to different light sources and pixel density of the spectrometer. The correction factor, R_{cor}, was determined by

$$R_{cor} = \frac{R_{true}}{R_{glass}} \tag{3.3}$$

Where R_{true} and R_{glass} are the true and in situ reflectance measurement of the bare substrate, respectively. If a transparent substrate is used, it is critical to measure the sample over a black material to eliminate the effects of the stage underneath. In this work the black material used was a heat resistance sheet of plastic made by Cookina.

The work related to the reflectance calibration and spectrum fitting was done by Kissan Mistry, a Ph.D. candidate at the University of Waterloo. The reflectance spectrum was fitted to the Tauc-Lorentz model [50] using the Levenberg-Marquardt algorithm [51]. The film thickness was extracted from one of the estimated parameters from the Tauc-Lorentz model, and the rest of the parameters were used to determine the extinction coefficient, which was then used to generate a Tauc plot to determine the bandgap. An initial guess of the parameters is required for the Levenberg-Marquardt algorithm as a starting point to find the optimal parameters. Since only ZnO films were produced, the initial guess for the parameters other than the thickness was held constant throughout the deposition as

they do not vary much. The initial guess for the thickness for each measurement was set to the optimal thickness of the previous measurement. An example of fitting the Tauc-Lorentz model and determining the bandgap from the Tauc plot is shown in Figure 3.6. The thickness was 225.3 nm, and the bandgap was 3.18 eV which agrees with the literature for ZnO [52].

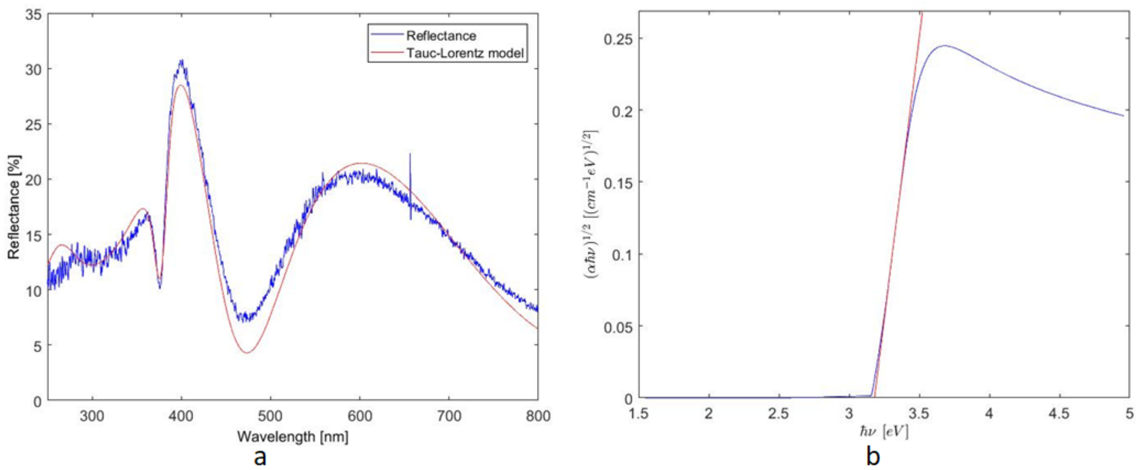

Figure 3.6: Reflectance spectrum fitted with the Tauc-Lorentz model (a) to determine thickness and Tauc plot (b) to determine bandgap

Nine ZnO films were deposited with in situ thickness measurements to train the ANN discussed in Chapter 4. Each film was deposited with 250 oscillations and varying deposition parameters to explore the parameter space of the AP-SALD system. The in situ measurements were recorded at zero oscillations to measure the bare substrate and at every third oscillation during depositions, thus, generating 84 unique training data for each film

produced.

In this work, only the precursor carrier flow rate and inert curtain flow rate were varied while all other deposition parameters (found in Table 3.2) were held constant. The total flow rate in each precursor channel in the reactor head (bubbler flow + carrier flow) was set to 50, 100 and 150 SCCM and the inert curtain flow rate was set to 125, 208 and 333 SCCM. These deposition parameters were chosen to observe the effects of precursor separation by varying the flow rate of the precursors and inert curtain.

Table 3.2: Fixed deposition parameters during the collection of training data

Deposition parameter	**Fixed value**
H_2O bubbler flow rate	50 SCCM
DEZ bubbler flow rate	25 SCCM
Substrate temperature	150°C
Oscillation speed	10 mm/s
Number of oscillations	250
Reactor head separation	100 μm

A plot of the film thickness as a function of the number of oscillation for all nine films is presented in Figure 3.7. Each plot is presented separately in Appendix B. The growth rate of each deposition is shown above each corresponding plot.

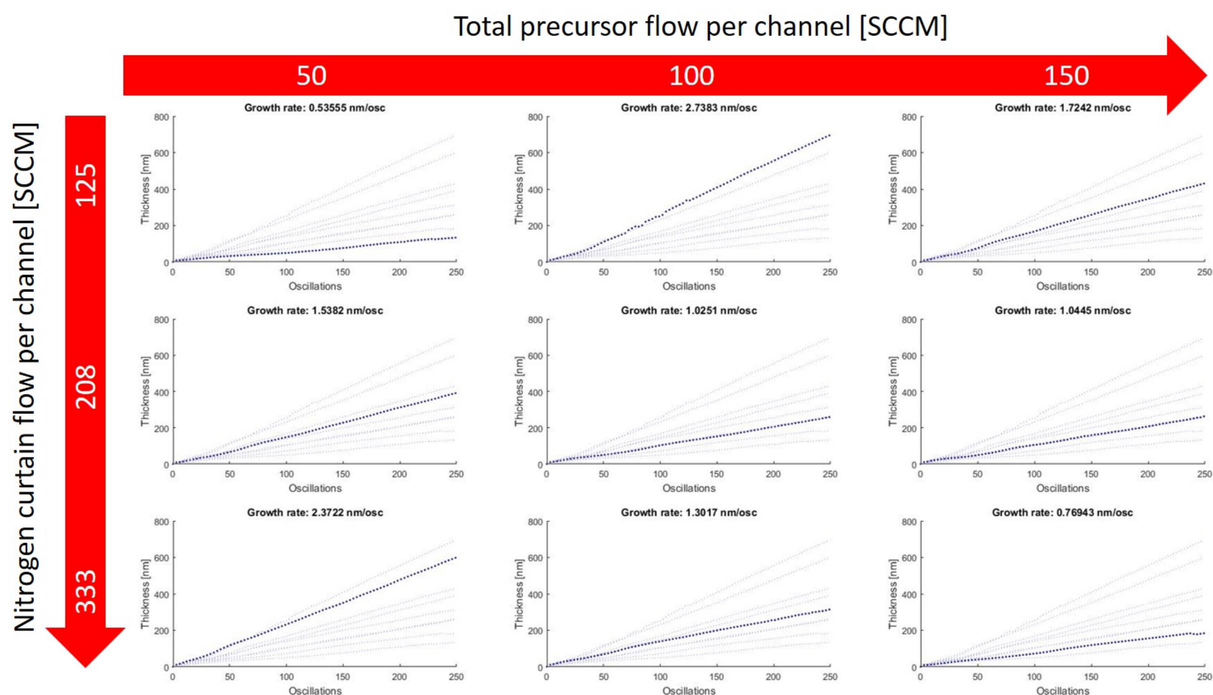

Figure 3.7: Film thickness as a function of the number of oscillation of the neural network training data obtained using the in situ optical measurement technique

All nine films had growth rates greater than the growth rates of 0.18-0.19 nm per cycle that was reported in the literature for conventional ALD of ZnO [23,48,53]. Keep in mind the growth rates in this work are expressed as nanometers per oscillation which is double the equivalent ALD growth rates because each oscillation results in two ALD cycles. The higher growth rates suggest that all the nine films were deposited in CVD mode because one ALD cycle will result in a monolayer due to the self-limiting reaction of the precursors, however, in CVD, the reaction is not self-limiting which leads to a thicker film. From

the leftmost column (precursor flow: 50 SCCM) of Figure 3.7, the film thickness increases with the nitrogen curtain flow rate suggesting the nitrogen curtain is causing turbulence under the reactor head which leads to the mixing of the precursor gases. Contrarily, the rightmost column (precursor flow: 150 SCCM) of Figure 3.7, shows the film thickness decreases as the flow rate for the nitrogen curtain increases which may be explained by the possibility that there was already turbulence under the reactor head with the lowest flow rates (precursor: 150 SCCM, nitrogen: 125 SCCM). Increasing the nitrogen curtain may then have diluted the precursor gases which resulted in a decreased growth rate. The lowest flow in the middle column (precursor: 100 SCCM, nitrogen: 125 SCCM) has an unusually high growth rate which suggests there was a source of error during the deposition of that particular film. All deposition parameters were computer controlled except for the reactor head separation which was manually adjusted (See Figure 2.1). It was highly likely the reactor head separation for that particular film was greater than the other depositions which allowed for more mixing of the precursor gases and resulted in a thicker film.

Nonetheless, the data shown in Figure 3.6 and 3.7 clearly demonstrates that accurate film thicknesses and bandgaps can be measured while the films are growing, using the in situ optical characterization technique developed for the AP-SALD system. In addition to providing valuable information about the film properties and nature of the film growth in the AP-SALD system, the in situ electrical and optical measurements provide a wealth of training data for an ANN.

Chapter 4

Artificial Neural Network

To demonstrate the ability to generate deposition parameters given a set of film properties, an ANN first needs to be trained to model the dynamics of the AP-SALD. Once the ANN can accurately represent the AP-SALD, an inverse neural network algorithm will be implemented to search for the corresponding depositions parameters given a set of film properties.

4.1 Architecture

A simple shallow feedforward ANN was developed to demonstrate the ability to utilize an AP-SALD system enhanced with in situ characterization tools for the purpose of film property control, high throughput screening, and new material discovery. While the AP-SALD system discussed earlier in this paper was designed to accommodate five different metal precursors to produce a wide range of materials, this work will only focus on ZnO films that were produced with DEZ and H_2O precursors. The ANN takes in a set of deposition parameters as inputs and outputs the film properties. The ANN will effectively be a model of the AP-SALD system. The network has three input neurons, one output neuron, and 25 hidden neurons. The sigmoid function and linear function were used as the activation functions for the hidden and output neurons, respectively.

4.2 Training

The set of training data used to train the ANN was the same data set discussed in Chapter 3, Section 3.2. The training data were carefully chosen to include the extreme ends of the deposition parameters because the ANN is more accurate when interpolating than extrapolating [54]. The nine films produced each had 84 thickness measurements which lead to 756 unique training data to train the ANN.

The training data were divided into two disjoint sets: a training set and a test set. The split between the training and the test was 85 and 15%, respective. The training set was used to train the ANN and the test set, which was completely independent of training the ANN, was used to demonstrate the ANN's ability to generalize to new data and tune the ANN's hyperparameters such as the number of hidden layers and the training algorithm. Depending on the training algorithm, sometimes a validation set is needed to determine when to stop training to prevent overfitting. Overfitting occurs when the ANN fits the training data so well, it loses its ability to generalize to new data. The ANN is essentially "memorizing" the training data instead of "learning" from it [55]. In this case, a validation set was not used because the Bayesian regularization backpropagation algorithm [56] was used as the training algorithm as it was proven experimentally to give the best performance. A regularization parameter was used to prevent overfitting by penalizing complex models and thus allow the model to better generalize to new data.

The ANN stopped training after 1000 epochs with the training set and test set having a mean squared error (MSE) of 0.9792 and 1.3287, respectively. An epoch is defined as passing the entire training set forward and backward through the ANN once. The mean

squared error of the two sets are small in magnitude and reasonably close to each other indicating the ANN was trained well and can generalize to new data. A plot of the ANN fitting the in situ thickness data as a function of the number of oscillations for 100 SCCM precursor flow and 208 SCCM nitrogen curtain flow is shown in Figure 4.1.

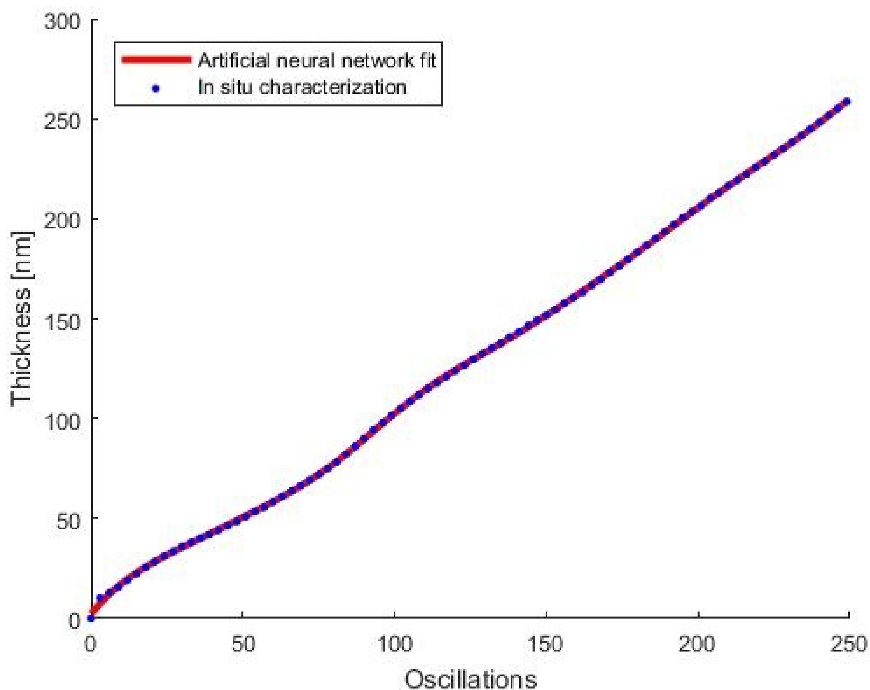

Figure 4.1: A plot of an ANN fitting the in situ thickness measurement with 100 SCCM of precursor flow and 208 SCCM of nitrogen curtain flow

Figure 4.2 shows the ANN fitting to the thickness of all nine films at oscillation number 249. The surface is relatively smooth indicating the ANN did not overfit the training data. Additional plots highlighting the performance of the ANN such as the training performance as a function of epochs (Figure C.1), the error histogram (Figure C.2) and the regression

plots (Figure C.3) can be found in Appendix C.

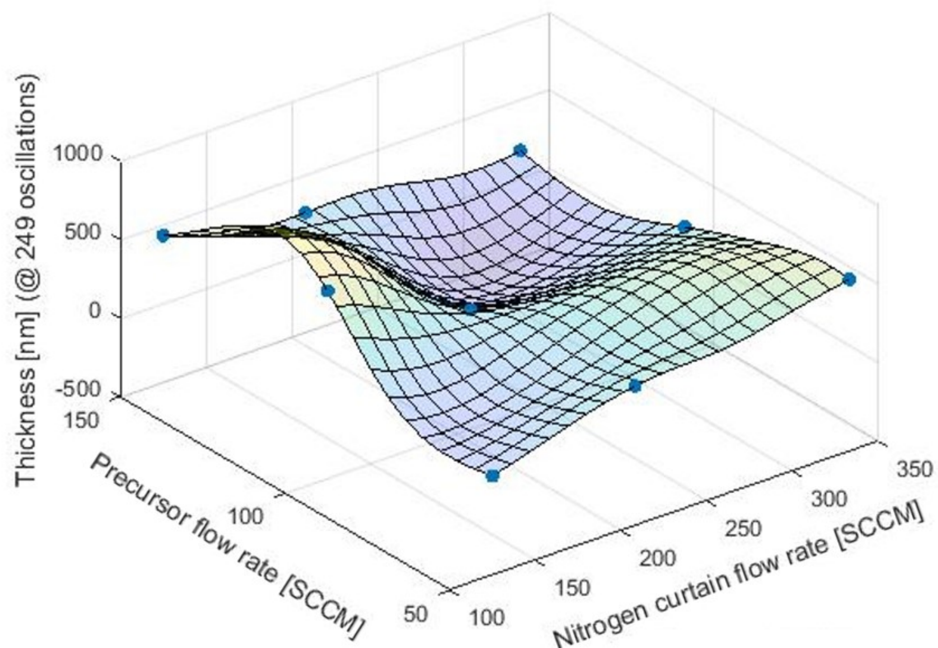

Figure 4.2: A plot of an ANN fitting the in situ thickness measurement of all nine films at oscillation number 249

4.3 Inverse Neural Network

An ANN that can predict the film properties given a set of deposition parameters does not provide much useful information. It would be more interesting to have the reverse model where given a set of film properties, the model will output the set of deposition parameters to use to produce a film with said properties. Training the ANN with the input and output swapped will create a one to many mapping in which there are no closed-form expressions [57]. In the case of the ANN trained in Section 4.2, there are multiple (possibly infinite) sets of precursor flow, nitrogen curtain flow and the number of oscillations triplets that yield the same thickness. Therefore, given a film thickness, an ANN would not be able to output every set of precursor flow, nitrogen curtain flow and the number of oscillations that will yield said thickness. In fact, when there are more inputs than output, the inverse of the ANN is generally not unique [58].

A simple solution to this problem is to find a single set of inputs given a set of outputs. Doing so will not generate all the inputs, but it will significantly reduce the complexity of the inverse algorithms because the search will terminate as soon as the first one is found. The Williams, Linden, and Kindermann (WLK) inversion algorithm, which was first introduced by Willams [59] and later proposed by Linden and Kindermann [60] uses a gradient descent approach to converge onto the input of interest. Similar to the WLK inversion algorithm, the Levenberg-Marquardt algorithm [51] was used to solve Equation 4.1 with an iterative approach to find a set of inputs that will give the corresponding output.

$$(x_N^*, x_P^*, x_O^*) = \underset{(x_N, x_P, x_O)}{\arg\min} \left(f_{ANN}(x_N, x_P, x_O) - d\right)^2 \quad (4.1)$$

Where (x_N^*, x_P^*, x_O^*) is the set of inputs (x_N is the nitrogen curtain flow, x_P is the precursor flow, and x_O is the number of oscillations) that will make the output of the ANN, $f_{ANN}(\cdot)$, approximately equal to the desired thickness, d.

The regression plot and the error histogram to highlight the performance of the inverse neural network algorithm can be found in Figure 4.3. The Levenberg-Marquardt algorithm predicted the inputs for 200 uniformly distributed random thicknesses between 0 and 700 nm. An initial guess is required for the Levenberg-Marquardt algorithm as the starting point. The initial guesses for the Levenberg-Marquardt algorithm were also randomly chosen according to the uniform distribution. The Levenberg-Marquardt algorithm occasionally converges to a local minimum resulting in a poor prediction of the input parameters. An additional condition was implemented to verify the prediction to prevent convergence to the false local minimum. If the prediction is poor, one can generate a new initial guess and rerun the algorithm. A desired thickness of 200 nm was inputted into the inverse neural network algorithm, and a nitrogen curtain flow rate of 165 SCCM, precursor flow rate of 93 SCCM, and 140 oscillations were returned by the algorithm. The values suggested by the inverse neural network algorithm are reasonable based on previous experience with the AP-SALD system. The performance of the inverse neural network algorithm is shown in Figure 4.3. On the left (a) is the regression plot where the x-axis is the desired thickness that was fed into the inverse neural network algorithm. The y-axis is the true output of the inverse neural network algorithm based on the deposition parameters

it found. Thus, a perfect fit will result in all data points on the Y=T line (slope of 1 and y-intercept of 0) and an R-value of 1. The plot of the right (b) is the error histogram of the inverse neural network algorithm. The x-axis is the error and is divided into 11 bins. The size of each bin is $\sim 1.43 \cdot 10^{-8}$. The error of each data point is sorted into the corresponding bins. The closer the instances of error are around the zero error line, the better the fit. The inverse neural network algorithm performed very well since in Figure 4.3(a) the R-value was 1. The performance was also confirmed by the error histogram shown in Figure 4.3(b) since almost all the data points are in the bin containing zero error and the MSE was $2.5851 \cdot 10^{-14}$.

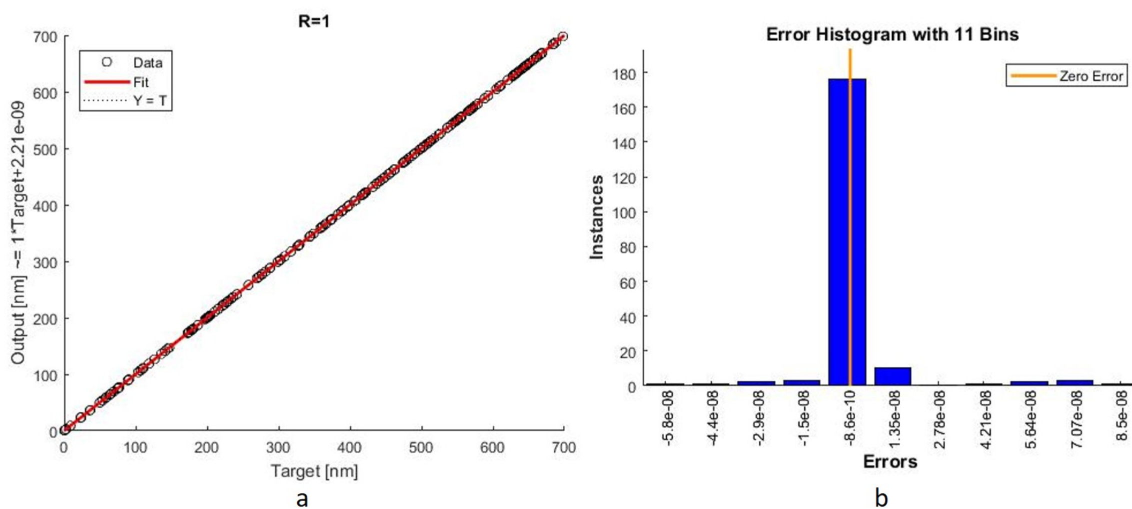

Figure 4.3: The regression plot (a) and the error histrogram (b) of the inverse neural network algorithm

It has been demonstrated that an ANN can be trained based on in situ characterization data

from the AP-SALD system. In the first instance was shown with varying two flows and the number of oscillations as inputs (defined using the control system discussed in Chapter 2) and film thickness as the output (measured using the in-situ optical measurements discussed in Chapter 3). The ANN allows the prediction of the film thickness for any combination of these inputs. More importantly, the presented inverse neural network algorithm enables the prediction of inputs that can be used to obtain the desired output (film thickness).

Chapter 5

Conclusion

An AP-SALD system was successfully designed and built from scratch entirely by co-op and graduate students in Dr. Kevin Musselman's lab at the University of Waterloo. Analog I/O modules from Opto 22 were used to control the flow rate of all the gases in the AP-SALD system. Digital output modules were used to control the pneumatic valves to shut off the appropriate gas lines. A time-optimal 5th order trajectory and a drift algorithm was implemented to oscillate the stage under the reactor head during depositions. A PI temperature feedback control with feedforward and anti-windup algorithm were developed to heat the substrate to promote reaction on the surface. The temperature settling time of the system was significantly below the time required to set up the AP-SALD. All the control software and HMI were written in PAC Control Basic and PAC Display. The AP-SALD system was able to consistency produce ZnO films with DEZ and H_2O as precursors. In situ electrical and optical characterization tools were developed to monitor the resistivity, thickness and bandgap during the growth of the film. A relay circuit was designed to route

the electrodes from an SMU to a custom PCB which was designed to act as the electrodes and substrate for resistivity measurements. From the in situ resistivity measurements, ZnO grows in an island formation before coalescing to form a continuous film. Reflectance spectroscopy was used to determine the film thickness and bandgap with the Tauc-Lorentz model and Tauc plot. As a proof of principle, a feedforward shallow ANN was trained with the in situ characterization data to relate the deposition parameters to the film thickness. A simple inverse neural network algorithm was implemented to generate deposition recipes by providing the deposition parameters to achieve the desired film thickness.

5.1 Future Work

Many improvements can be made to the AP-SALD system and the ANN. First off the manual reactor head separation adjustment should be computer controlled to improve on the repeatability of the depositions.

In this work, only ZnO films were studied. It would be interesting to study other materials such as tungsten oxide (WO_3), tin oxide (SnO_2) and aluminum oxide (Al_2O_3) using other precursors. The different precursors can be used as dopants by either mixing the precursor gases in the lines before exiting the reactor head or by introducing different precursor gases every few oscillations.

Regarding in situ characterization, more film properties such as refractive index, dielectric constant and absorption constant can be studied and ultimately be used to train the ANN. The PCB should be redesigned to prevent turbulence under the reactor head by eliminating the need for Kapton tape to mask off the copper traces.

Gradient films can also be made by setting the reactor head separation to be greater on one side or design a new reactor head all together to change the precursor flow characteristics. The PCB was already designed to allow for gradient resistivity measurements. However, additional reflectance probes and a multiplexer would have to be used to capture reflectance measurements across the gradient.

The training data in this work kept a lot of deposition parameters constant. It would be interesting to see the effects of varying all the parameters on the film properties. All the improvements discussed so far will generate a considerable parameter space (e.g., multi-component alloys). A more sophisticated ANN such as a recurrent neural network, a

convolutional neural network, a deep neural network or any combination of the previous may have to be used to model the AP-SALD system.

A more complex inverse neural network algorithm can be developed to generate all the inputs associated with any particular output. It may also be important to develop an intelligent inverse neural network algorithm where only the optimal set of inputs will be returned. The optimality of the inputs can be ranked based on the deposition time and the total volume of precursors used to create the film. Finding more optimal deposition parameters that achieve the same film properties will be crucial in large-scale manufacturing where cost reduction is critical.

Lastly, it would be interesting to determine the ALD window (i.e., deposition conditions for which true ALD, rather than CVD, is obtained) of the AP-SALD system. A new ANN can be trained with the deposition parameters as its inputs and the growth rate as its output. When the growth rate is independent of the deposition parameters, the ALD process is achieved [23]. In true ALD, the reactants are self-limiting thus the reaction mechanism will only depend on the reactants and not on the deposition parameters. With a well trained ANN, determining the ALD window can be done by simply analyzing the Jacobian of the ANN.

References

[1] S. M. George, “Atomic layer deposition: an overview,” *Chemical reviews*, vol. 110, no. 1, pp. 111–131, 2009.

[2] T. Weckman and K. Laasonen, “Atomic layer deposition of zinc oxide: Diethyl zinc reactions and surface saturation from first-principles,” *The Journal of Physical Chemistry C*, vol. 120, no. 38, pp. 21460–21471, 2016.

[3] F. Lee, S. Marcus, E. Shero, G. Wilk, J. Swerts, J. W. Maes, T. Blomberg, A. Delabie, M. Gros-Jean, and E. Deloffre, “Atomic layer deposition: an enabling technology for microelectronic device manufacturing,” in *Advanced Semiconductor Manufacturing Conference, 2007. ASMC 2007. IEEE/SEMI*, pp. 359–365, IEEE, 2007.

[4] P. F. Carcia, R. McLean, M. Reilly, M. Groner, and S. George, “Ca test of al 2 o 3 gas diffusion barriers grown by atomic layer deposition on polymers,” *Applied physics letters*, vol. 89, no. 3, p. 031915, 2006.

[5] X. Meng, X.-Q. Yang, and X. Sun, “Emerging applications of atomic layer deposition for lithium-ion battery studies,” *Advanced Materials*, vol. 24, no. 27, pp. 3589–3615,

2012.

[6] M. Cassir, A. Ringuedé, and L. Niinistö, "Input of atomic layer deposition for solid oxide fuel cell applications," *Journal of Materials Chemistry*, vol. 20, no. 41, pp. 8987–8993, 2010.

[7] J. R. Bakke, K. L. Pickrahn, T. P. Brennan, and S. F. Bent, "Nanoengineering and interfacial engineering of photovoltaics by atomic layer deposition," *Nanoscale*, vol. 3, no. 9, pp. 3482–3508, 2011.

[8] J. Van Delft, D. Garcia-Alonso, and W. Kessels, "Atomic layer deposition for photovoltaics: applications and prospects for solar cell manufacturing," *Semiconductor Science and Technology*, vol. 27, no. 7, p. 074002, 2012.

[9] P. Poodt, A. Lankhorst, F. Roozeboom, K. Spee, D. Maas, and A. Vermeer, "High-speed spatial atomic-layer deposition of aluminum oxide layers for solar cell passivation," *Advanced Materials*, vol. 22, no. 32, pp. 3564–3567, 2010.

[10] P. Poodt, D. C. Cameron, E. Dickey, S. M. George, V. Kuznetsov, G. N. Parsons, F. Roozeboom, G. Sundaram, and A. Vermeer, "Spatial atomic layer deposition: A route towards further industrialization of atomic layer deposition," *Journal of Vacuum Science & Technology A: Vacuum, Surfaces, and Films*, vol. 30, no. 1, p. 010802, 2012.

[11] A. Jain, Y. Shin, and K. A. Persson, "Computational predictions of energy materials using density functional theory," *Nature Reviews Materials*, vol. 1, no. 1, p. 15004, 2016.

[12] I. E. Castelli, T. Olsen, S. Datta, D. D. Landis, S. Dahl, K. S. Thygesen, and K. W. Jacobsen, "Computational screening of perovskite metal oxides for optimal solar light capture," *Energy & Environmental Science*, vol. 5, no. 2, pp. 5814–5819, 2012.

[13] I. E. Castelli, D. D. Landis, K. S. Thygesen, S. Dahl, I. Chorkendorff, T. F. Jaramillo, and K. W. Jacobsen, "New cubic perovskites for one-and two-photon water splitting using the computational materials repository," *Energy & Environmental Science*, vol. 5, no. 10, pp. 9034–9043, 2012.

[14] Y. Wu, P. Lazic, G. Hautier, K. Persson, and G. Ceder, "First principles high throughput screening of oxynitrides for water-splitting photocatalysts," *Energy & Environmental Science*, vol. 6, no. 1, pp. 157–168, 2013.

[15] P. Raccuglia, K. C. Elbert, P. D. Adler, C. Falk, M. B. Wenny, A. Mollo, M. Zeller, S. A. Friedler, J. Schrier, and A. J. Norquist, "Machine-learning-assisted materials discovery using failed experiments," *Nature*, vol. 533, no. 7601, p. 73, 2016.

[16] Y. Iwasaki, I. Takeuchi, V. Stanev, A. G. Kusne, M. Ishida, A. Kirihara, K. Ihara, R. Sawada, K. Terashima, H. Someya, *et al.*, "Machine-learning guided discovery of a high-performance spin-driven thermoelectric material," *arXiv preprint arXiv:1805.02303*, 2018.

[17] S. F. Nelson, D. H. Levy, L. W. Tutt, and M. Burberry, "Cycle time effects on growth and transistor characteristics of spatial atomic layer deposition of zinc oxide," *Journal of Vacuum Science & Technology A: Vacuum, Surfaces, and Films*, vol. 30, no. 1, p. 01A154, 2012.

[18] B. Ehrler, K. P. Musselman, M. L. Bohm, F. S. Morgenstern, Y. Vaynzof, B. J. Walker, J. L. MacManus-Driscoll, and N. C. Greenham, "Preventing interfacial recombination in colloidal quantum dot solar cells by doping the metal oxide," *Acs Nano*, vol. 7, no. 5, pp. 4210–4220, 2013.

[19] A. Illiberi, R. Scherpenborg, Y. Wu, F. Roozeboom, and P. Poodt, "Spatial atmospheric atomic layer deposition of al x zn1–x o," *ACS applied materials & interfaces*, vol. 5, no. 24, pp. 13124–13128, 2013.

[20] A. Illiberi, R. Scherpenborg, F. Roozeboom, and P. Poodt, "Atmospheric spatial atomic layer deposition of in-doped zno," *ECS Journal of Solid State Science and Technology*, vol. 3, no. 5, pp. P111–P114, 2014.

[21] K. P. Musselman, S. Albert-Seifried, R. L. Hoye, A. Sadhanala, D. Muñoz-Rojas, J. L. MacManus-Driscoll, and R. H. Friend, "Improved exciton dissociation at semiconducting polymer: Zno donor: Acceptor interfaces via nitrogen doping of zno," *Advanced functional materials*, vol. 24, no. 23, pp. 3562–3570, 2014.

[22] C. R. Ellinger and S. F. Nelson, "Selective area spatial atomic layer deposition of zno, al2o3, and aluminum-doped zno using poly (vinyl pyrrolidone)," *Chemistry of Materials*, vol. 26, no. 4, pp. 1514–1522, 2014.

[23] A. Illiberi, F. Roozeboom, and P. Poodt, "Spatial atomic layer deposition of zinc oxide thin films," *ACS applied materials & interfaces*, vol. 4, no. 1, pp. 268–272, 2011.

[24] A. S. Yersak, Y. C. Lee, J. A. Spencer, and M. D. Groner, "Atmospheric pressure spatial atomic layer deposition web coating with in situ monitoring of film thickness,"

Journal of Vacuum Science & Technology A: Vacuum, Surfaces, and Films, vol. 32, no. 1, p. 01A130, 2014.

[25] E. Langereis, S. Heil, H. Knoops, W. Keuning, M. Van de Sanden, and W. Kessels, "In situ spectroscopic ellipsometry as a versatile tool for studying atomic layer deposition," *Journal of Physics D: Applied Physics*, vol. 42, no. 7, p. 073001, 2009.

[26] D. N. Goldstein, J. A. McCormick, and S. M. George, "Al2o3 atomic layer deposition with trimethylaluminum and ozone studied by in situ transmission ftir spectroscopy and quadrupole mass spectrometry," *The Journal of Physical Chemistry C*, vol. 112, no. 49, pp. 19530–19539, 2008.

[27] M.-T. Ho, Y. Wang, R. Brewer, L. Wielunski, Y. Chabal, N. Moumen, and M. Boleslawski, "In situ infrared spectroscopy of hafnium oxide growth on hydrogen-terminated silicon surfaces by atomic layer deposition," *Applied Physics Letters*, vol. 87, no. 13, p. 133103, 2005.

[28] M. Schuisky, J. Elam, and S. George, "In situ resistivity measurements during the atomic layer deposition of zno and w thin films," *Applied Physics Letters*, vol. 81, no. 1, pp. 180–182, 2002.

[29] E. Langereis, H. Knoops, A. Mackus, F. Roozeboom, M. Van de Sanden, and W. Kessels, "Synthesis and in situ characterization of low-resistivity ta n x films by remote plasma atomic layer deposition," *Journal of Applied Physics*, vol. 102, no. 8, p. 083517, 2007.

[30] J.-S. Na, G. Scarel, and G. N. Parsons, "In situ analysis of dopant incorporation, activation, and film growth during thin film zno and zno: Al atomic layer deposition," *The Journal of Physical Chemistry C*, vol. 114, no. 1, pp. 383–388, 2009.

[31] B. K. Bose, "Neural network applications in power electronics and motor drivesan introduction and perspective," *IEEE Transactions on Industrial Electronics*, vol. 54, no. 1, pp. 14–33, 2007.

[32] M. A. Shahin, M. B. Jaksa, and H. R. Maier, "Artificial neural network applications in geotechnical engineering," *Australian geomechanics*, vol. 36, no. 1, pp. 49–62, 2001.

[33] A. Miller, B. Blott, *et al.*, "Review of neural network applications in medical imaging and signal processing," *Medical and Biological Engineering and Computing*, vol. 30, no. 5, pp. 449–464, 1992.

[34] B. K. Wong and Y. Selvi, "Neural network applications in finance: a review and analysis of literature (1990–1996)," *Information & Management*, vol. 34, no. 3, pp. 129–139, 1998.

[35] C. Robert, C. Guilpin, and A. Limoge, "Review of neural network applications in sleep research," *Journal of Neuroscience methods*, vol. 79, no. 2, pp. 187–193, 1998.

[36] Y.-D. Ko, H. S. Kang, M.-C. Jeong, S. Y. Lee, J.-M. Myoung, and I. Yun, "Neural network based modeling for the growth rate of zno thin films on the pulsed laser deposition," in *Future of Electron Devices, 2004. International Meeting for*, pp. 79–80, IEEE, 2004.

[37] Y.-D. Ko, P. Moon, C. E. Kim, M.-H. Ham, J.-M. Myoung, and I. Yun, "Modeling and optimization of the growth rate for zno thin films using neural networks and genetic algorithms," *Expert Systems with Applications*, vol. 36, no. 2, pp. 4061–4066, 2009.

[38] K. Hornik, M. Stinchcombe, and H. White, "Multilayer feedforward networks are universal approximators," *Neural networks*, vol. 2, no. 5, pp. 359–366, 1989.

[39] K. Erkorkmaz, "Lecture notes in precision control systems," September 2016.

[40] Alzaydi, Ammar, "Time-optimal trajectory generation for 5-axis on-the-fly laser drilling," Master's thesis, 2011.

[41] K. D. Nguyen, T.-C. Ng, and I.-M. Chen, "On algorithms for planning s-curve motion profiles," *International Journal of Advanced Robotic Systems*, vol. 5, no. 1, p. 11, 2008.

[42] S. F. Barrett and D. J. Pack, *Microcontrollers fundamentals for engineers and scientists.* Morgan & Claypool, 2006.

[43] G. Cohen and G. Coon, "Theoretical investigation of retarded control.," *Trans. Amer. Soc. Mech. Eng.*, vol. 75, pp. 827–834, 1953.

[44] A. Packard, "Lecture notes in dynamic systems and feedback," May 2015.

[45] T.-T. Tay, I. Mareels, and J. B. Moore, "High performance control (systems & control: Foundations & applications)," 1997.

[46] H.-D. Liu, Y.-P. Zhao, G. Ramanath, S. Murarka, and G.-C. Wang, "Thickness dependent electrical resistivity of ultrathin (< 40 nm) cu films," *Thin Solid Films*, vol. 384, no. 1, pp. 151–156, 2001.

[47] V. Lujala, J. Skarp, M. Tammenmaa, and T. Suntola, "Atomic layer epitaxy growth of doped zinc oxide thin films from organometals," *Applied surface science*, vol. 82, pp. 34–40, 1994.

[48] S. K. Kim, C. S. Hwang, S.-H. K. Park, and S. J. Yun, "Comparison between zno films grown by atomic layer deposition using h2o or o3 as oxidant," *Thin Solid Films*, vol. 478, no. 1-2, pp. 103–108, 2005.

[49] G. Moona, P. Kapruwan, R. Sharma, and V. Ojha, "Silicon wafer surface reflectance investigations by using different surface texturing parameters," *Proceedings of the National Academy of Sciences, India Section A: Physical Sciences*, pp. 1–7, 2017.

[50] G. Jellison Jr and F. Modine, "Parameterization of the optical functions of amorphous materials in the interband region," *Applied Physics Letters*, vol. 69, no. 3, pp. 371–373, 1996.

[51] D. W. Marquardt, "An algorithm for least-squares estimation of nonlinear parameters," *Journal of the society for Industrial and Applied Mathematics*, vol. 11, no. 2, pp. 431–441, 1963.

[52] V. Srikant and D. R. Clarke, "On the optical band gap of zinc oxide," *Journal of Applied Physics*, vol. 83, no. 10, pp. 5447–5451, 1998.

[53] E. Guziewicz, I. Kowalik, M. Godlewski, K. Kopalko, V. Osinniy, A. Wójcik, S. Yatsunenko, E. Łusakowska, W. Paszkowicz, and M. Guziewicz, "Extremely low temperature growth of zno by atomic layer deposition," *Journal of Applied Physics*, vol. 103, no. 3, p. 033515, 2008.

[54] E. Barnard and L. Wessels, "Extrapolation and interpolation in neural network classifiers," *IEEE Control Systems*, vol. 12, no. 5, pp. 50–53, 1992.

[55] M. A. Nielsen, *Neural Networks and Deep Learning*. Determination Press, 2015.

[56] D. J. MacKay, "Bayesian interpolation," *Neural computation*, vol. 4, no. 3, pp. 415–447, 1992.

[57] A. Dua, "Inversion of neural networks: A solution to the problems encountered by a steel corporation," May 2000.

[58] C. A. Jensen, R. D. Reed, R. J. Marks, M. A. El-Sharkawi, J.-B. Jung, R. T. Miyamoto, G. M. Anderson, and C. J. Eggen, "Inversion of feedforward neural networks: Algorithms and applications," *Proceedings of the IEEE*, vol. 87, no. 9, pp. 1536–1549, 1999.

[59] R. J. Williams, "Inverting a connectionist network mapping by backpropagation of error," in *8th Annual Conf. Cognitive Sci. Soc.*, 1986.

[60] J. Kindermann and A. Linden, "Inversion of neural networks by gradient descent," *Parallel computing*, vol. 14, no. 3, pp. 277–286, 1990.

APPENDICES

Appendix A

AP-SALD Construction

A.1 AP-SALD Human Machine Interface

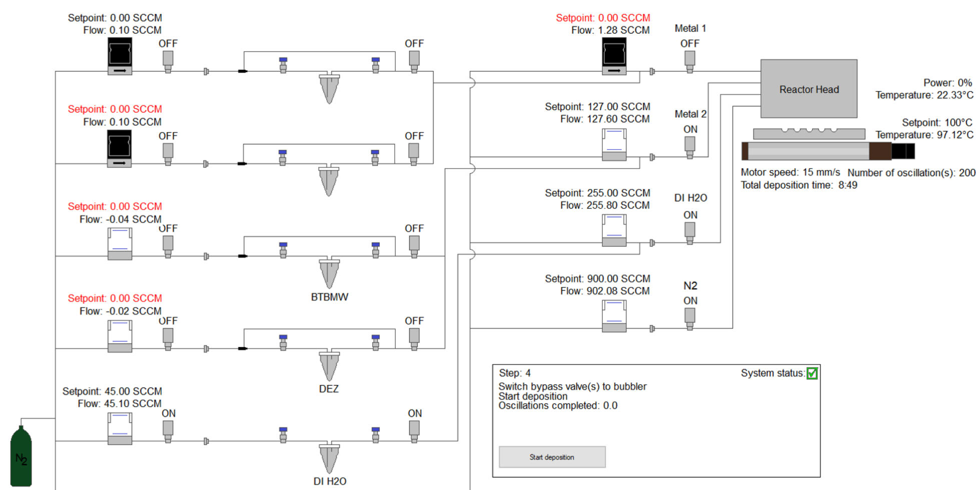

Figure A.1: The human machine interface of the AP-SALD system

A.2 Opto 22 Products

Table A.1: Opto 22 I/O modules and their usage in the AP-SALD system

Opto 22 products	**Description**	**AP-SALD Usage**
SNAP-PAC-R1	Controller + brain	Runs the control software and interfaces with I/O modules
SNAP-PAC-EB1	Brain	Interfaces with I/O modules
SNAP-PAC-RCK16	16 slot module rack	Physically and electrically connects I/O modules
SNAP-AIV-8/4	Analog input	Flow-meter feedback
SNAP-AOV-25	Analog output	Flow-meter setpoint
SNAP-ODC5-i	Digital output	Control pneumatic valves via manifold
SNAP-AITM-4i	Thermocouple input	Heated stage temperature feedback
SNAP-SCM-ST2	Pulse & direction digital output	Motor speed and direction command
SNAP-SCM-485-422	Serial communication module	Motor drive feedback
SNAP-IDC5-SW-NC	Switch input module	Read limit and enable switches
SNAP-AOD-29	Time proportional digital output	PWM control for the heated stage
SNAP-IDC5-SW	Switch input module	Physical motor control buttons
SNAP-ODC5SNK	Digital output Module	In situ electrical relay select
SNAP-IDC5-SW	Switch input module	Stage leveling tool
SNAP-ODC5-i	Digital output	Light source shutter control

A.3 Flow Meters Details

Table A.2: Flow meter operating ranges

Flow meter	**Operating range [sccm]**
Water bubbler	0 - 200
Metal bubbler	0 - 50
Precursor carrier	0 - 500
Nitrogen carrier	0 - 2000

Table A.3: Pinout for the flow meters and the Opto 22 I/O modules

Pin description	**Brooks 4850**	**Sierra SmartTrak**	**SNAP-AIV-8/4**	**SNAP-AOV-25**
Power supply (24VDC)	5	5	-	-
Ground	9	6	-	-
Setpoint voltage	8	3	-	2,6
Setpoint voltage return	1	4	-	3,7
Flow voltage	2	1	1,3,5,7	-
Flow voltage return	10	2	2,4,6,8	-

A.4 Pneumatic Valves Details

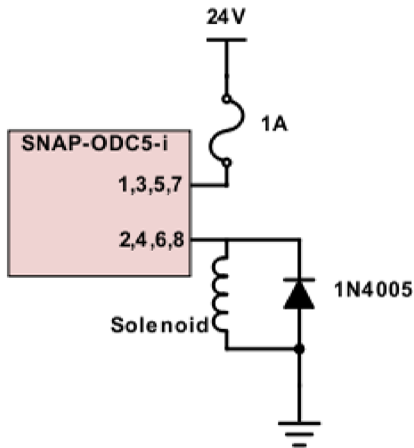

Figure A.2: Schematic diagram of the solenoid circuit

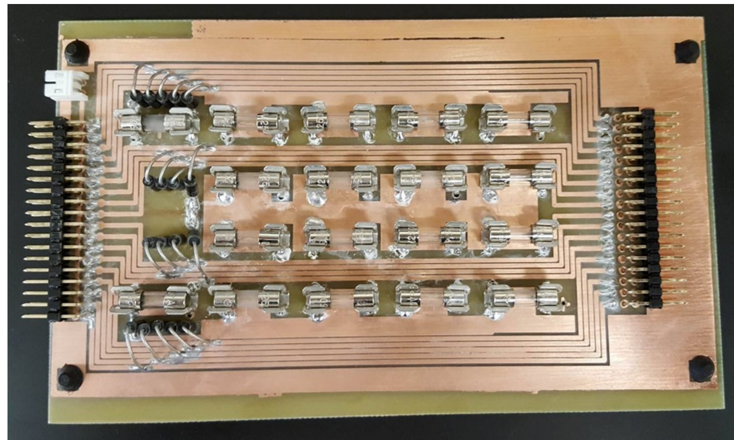

Figure A.3: Solenoid circuit used to control the pneumatic manifold

A.5 Servo Drive Details

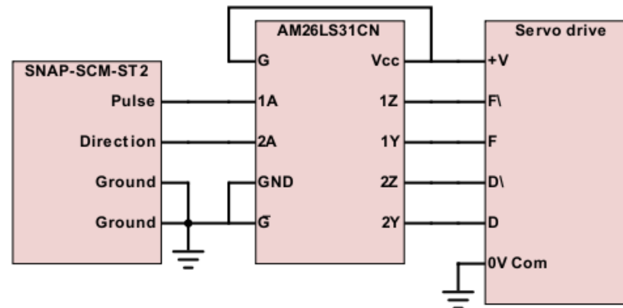

Figure A.4: Schematic diagram of the differential line driver used to convert the signals from the SNAP-SCM-ST2 to the servo drive

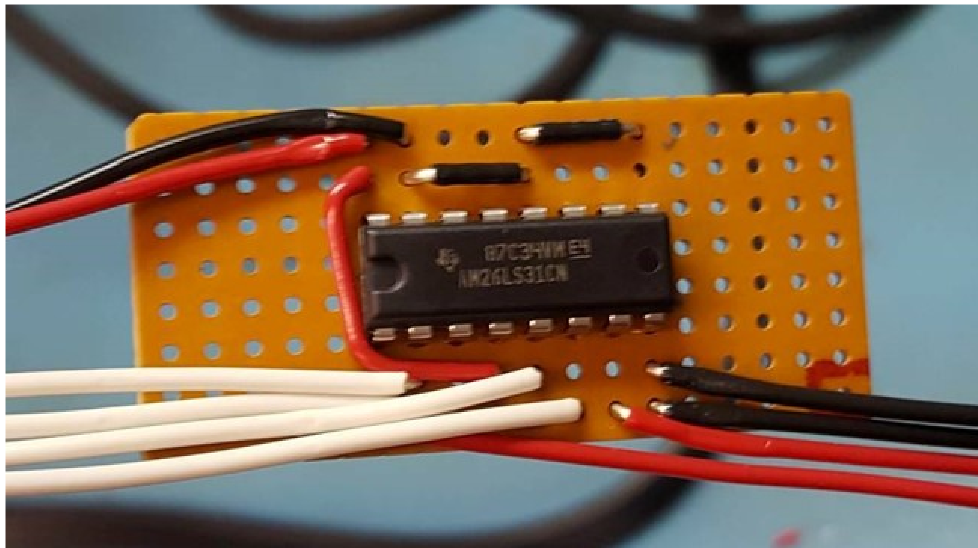

Figure A.5: Differential line driver used to send velocity commands to the servo drive

A.6 Motor Trajectory Details

The equations of the substrate trajectory are given below. Where $j(t)$ is the jerk or the rate of change of acceleration, $a(t)$ is the acceleration, $v(t)$ is the velocity and $x(t)$ is the position of the substrate. J_{max} and A_{max} were chosen to be as large as possible while staying within the tolerances of the motor assembly. L is the travel length of the substrate and V_d is the desired velocity in the constant velocity region. A negative T_4 means the trajectory is kinematically infeasible and L or V_d should be adjusted accordingly.

$$
j(t) = \begin{cases} -6\frac{A}{T_1^3}t^2 + 6\frac{A}{T_1^2}t, & t_0 \le t \le t_1 \\ 0, & t_1 < t \le t_2 \\ 6\frac{A}{T_1^3}(t-t_2)^2 - 6\frac{A}{T_1^2}(t-t_2), & t_2 < t \le t_3 \\ 0, & t_3 < t \le t_4 \\ 6\frac{A}{T_1^3}(t-t_4)^2 - 6\frac{A}{T_1^2}(t-t_4), & t_4 < t \le t_5 \\ 0, & t_5 < t \le t_6 \\ -6\frac{A}{T_1^3}(t-t_6)^2 + 6\frac{A}{T_1^2}(t-t_6), & t_6 < t \le t_7 \end{cases} \tag{A.1}
$$

$$
a(t) = \begin{cases} -2\frac{A}{T_1^3}t^3 + 3\frac{A}{T_1^2}t^2, & t_0 \le t \le t_1 \\ A, & t_1 < t \le t_2 \\ 2\frac{A}{T_1^3}(t-t_2)^3 - 3\frac{A}{T_1^2}(t-t_2)^2 + A, & t_2 < t \le t_3 \\ 0, & t_3 < t \le t_4 \\ 2\frac{A}{T_1^3}(t-t_4)^3 - 3\frac{A}{T_1^2}(t-t_4)^2, & t_4 < t \le t_5 \\ -A, & t_5 < t \le t_6 \\ -2\frac{A}{T_1^3}(t-t_6)^3 + 3\frac{A}{T_1^2}(t-t_6)^2 - A, & t_6 < t \le t_7 \end{cases} \tag{A.2}
$$

$$v(t) = \begin{cases} -\frac{1}{2}\frac{A}{T_1^3}t^4 + \frac{A}{T_1^2}t^3, & t_0 \le t \le t_1 \\ A(t-t_1) + \frac{1}{2}AT_1, & t_1 < t \le t_2 \\ \frac{1}{2}\frac{A}{T_1^3}(t-t_2)^4 - \frac{A}{T_1^2}(t-t_2)^3 + A(t-t_2) + \frac{1}{2}AT_1 + AT_2, & t_2 < t \le t_3 \\ AT_1 + AT_2, & t_3 < t \le t_4 \\ \frac{1}{2}\frac{A}{T_1^3}(t-t_4)^4 - \frac{A}{T_1^2}(t-t_4)^3 + AT_1 + AT_2, & t_4 < t \le t_5 \\ -A(t-t_5) + \frac{1}{2}AT_1 + AT_2, & t_5 < t \le t_6 \\ -\frac{1}{2}\frac{A}{T_1^3}(t-t_6)^4 + \frac{A}{T_1^2}(t-t_6)^3 - A(t-t_6) + \frac{1}{2}AT_1, & t_6 < t \le t_7 \end{cases} \tag{A.3}$$

$$x(t) = \begin{cases} -\frac{2}{5}\frac{1}{T_1^3}t^5 + \frac{1}{T_1^2}t^4, & t_0 \le t \le t_1 \\ \frac{1}{2}A(t-t_1)^2 + \frac{1}{2}AT_1(t-t_1) + \frac{3}{20}AT_1^2, & t_1 < t \le t_2 \\ \frac{1}{10}\frac{A}{T_1^3}(t-t_2)^5 - \frac{1}{4}\frac{A}{T_1^2}(t-t_2)^4 + \frac{1}{2}A(t-t_2)^2 + (\frac{1}{2}AT_1 + AT_2)(t-t_2) + \frac{3}{20}AT_1^2 + \frac{1}{2}AT_2(T_1+T_2), & t_2 < t \le t_3 \\ (AT_1 + AT_2)(t-t_3) + \frac{1}{2}AT_1^2 + T_1(\frac{1}{2}AT_1 + AT_2) + \frac{1}{2}AT_2(T_1+T_2), & t_3 < t \le t_4 \\ \frac{1}{10}\frac{A}{T_1^3}(t-t_4)^5 - \frac{1}{4}\frac{A}{T_1^2}(t-t_4)^4 + (AT_2 + AT_1)(t-t_4) + \frac{1}{2}AT_1^2 + T_1(\frac{1}{2}AT_1 + AT_2) + T_4(AT_1 + AT_2) + \frac{1}{2}AT_2(T_1+T_2), & t_4 < t \le t_5 \\ -\frac{1}{2}A(t-t_5)^2 + (\frac{1}{2}AT_1 + AT_2)(t-t_5) + \frac{1}{2}AT_1^2 + T_1(\frac{1}{2}AT_1 + AT_2) + T_4(AT_1 + AT_2) + \frac{17}{20}AT_1^2 + AT_2T_1 + \frac{1}{2}A(T_1+T_2), & t_5 < t \le t_6 \\ -\frac{1}{10}\frac{A}{T_1^3}(t-t_6)^5 + \frac{1}{4}\frac{A}{T_1^2}(t-t_6)^4 - \frac{1}{2}A(t-t_6)^2 + \frac{1}{2}A(t-t_6) + \frac{1}{2}AT_1^2 + T_1(\frac{1}{2}AT_1 + AT_2) + T_4(AT_1 + AT_2) + \frac{17}{20}AT_1^2 + AT_2T_1 + AT_2(T_1+T_2), & t_6 < t \le t_7 \end{cases} \tag{A.4}$$

$$
\begin{aligned}
&t_0 = 0 && t_1 = T_1 && t_2 = T_1 + T_2 && t_3 = 2T_1 + T_2 \\
&t_4 = 2T_1 + T_2 + T_4 && t_5 = 3T_1 + T_2 + T_4 && t_6 = 3T_1 + 2T_2 + T_4 && t_7 = 4T_1 + 2T_2 + T_4
\end{aligned}
$$

$$
T_1 = \frac{3}{2}\frac{A}{J_{max}} \qquad A = \begin{cases} \sqrt{\frac{2}{3}J_{max}V_d}, \text{ if } \sqrt{\frac{2}{3}J_{max}V_d} \leq A_{max} \\ A_{max}, \text{ otherwise} \end{cases} \qquad T_2 = \begin{cases} 0, \text{ if } \sqrt{\frac{2}{3}J_{max}V_d} \leq A_{max} \\ \frac{V_d}{A} - T_1, \text{ otherwise} \end{cases}
$$

$$
T_4 = \frac{L}{V_d} - (2T_1 + T_2)
$$

A.7 Substrate Heater Details

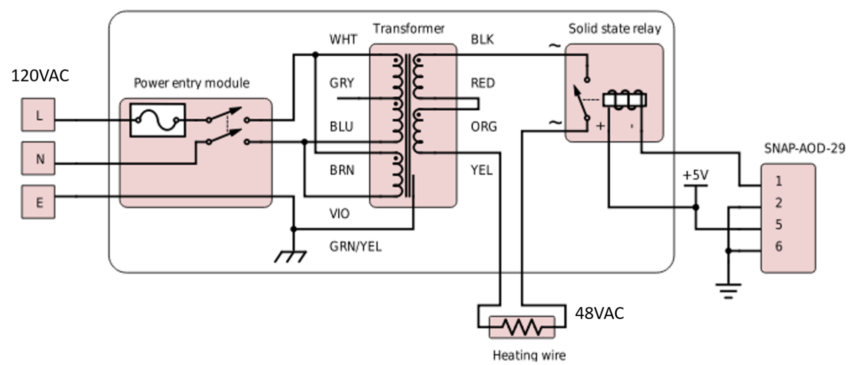

Figure A.6: Schematic of the resistive heating circuit to heat the stage during deposition

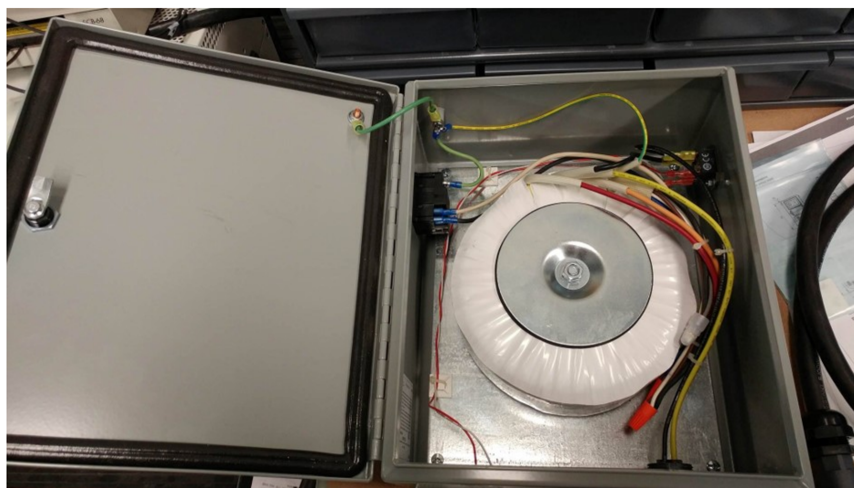

Figure A.7: Photo of the resistive heating circuit to heat the stage during deposition

Table A.4: Control parameters used in the substrate heater

	Controller gain (K_c)	**Integral time (T_i)**
P control	6.2774	-
PI control	5.4168	79.4887

The pseudocode for the anti-windup algorithm is detailed below:

Algorithm A.1: Anti-windup algorithm for the heating stage controls

```
1 if (CO ≥ 100% ∧ e > 0) ∨ (CO ≤ 0% ∧ e < 0) then
2     P control
3     Reset integrator
4 else
5     PI control
6 end if
```

Where CO is the controller output, e is the error, ∧ is the logical AND operator, and ∨ is the logical OR operator.

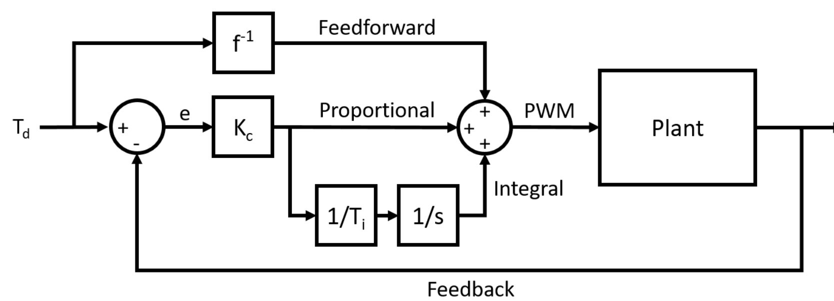

Figure A.8: Block diagram of the temperature controller used to set the temperature of the substrate in the AP-SALD system

Appendix B

In Situ Characterization Details

The pseudocode of an exponential search to find a suitable integration time is given in below. In line 12, the middle element was chosen differently than in a typical binary search algorithm. Assuming the time to capture a spectrum is exactly the integration time and the probability distribution of the suitable integration time is uniformly distributed between L and H, setting M as in line 12 will ensure the expected capture time will be

the same whether the suitable integration time is greater than or less than M.

Algorithm B.1: Exponential search to find a suitable integration time

```
1  LB ← 0.8*saturationLimit
2  UB ← 0.9*saturationLimit
3  Function ExponentialSearch:
4      b ← 1
5      do
6          b ← b*2
7          setIntegrationTime(b)
8          maxInt ← getMaxIntensity
9      while maxInt < LB
10 return BinarySearch(b/2,b)

11 Function BinarySearch(L,H):
12     M← sqrt((L^2+H^2)/2)
13     setIntegrationTime(M)
14     if getMaxIntensity ≤ UB ∧ getMaxIntensisty ≥ LB then
15         return M
16     else if getMaxIntensity < LB then
17         return BinarySearch(M,H)
18     else
19         return BinarySearch(L,M)
20     end if
```

All the figures below are deposited with the deposition parameters discussed in Chapter 3,

Section 3.2.

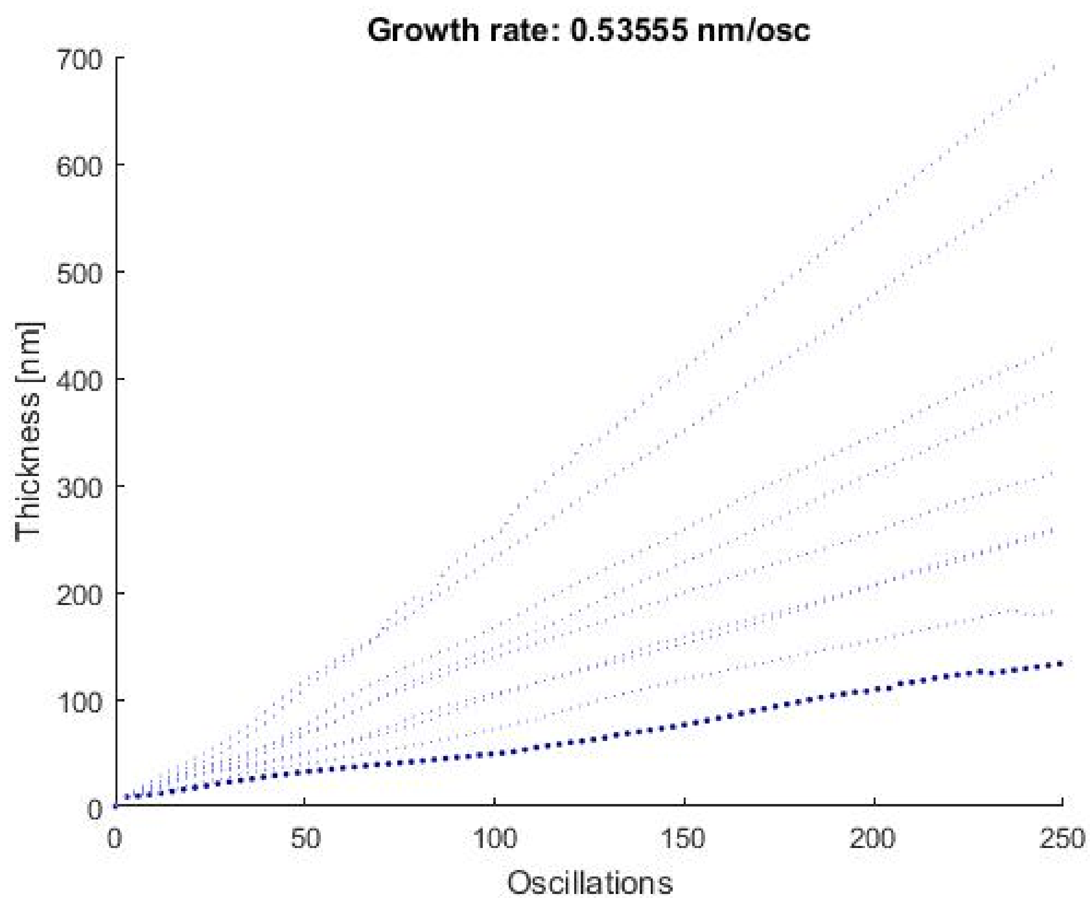

Figure B.1: Thickness as a function of number of oscillations deposited with 50 SCCM of precursor and 125 SCCM of nitrogen curtain

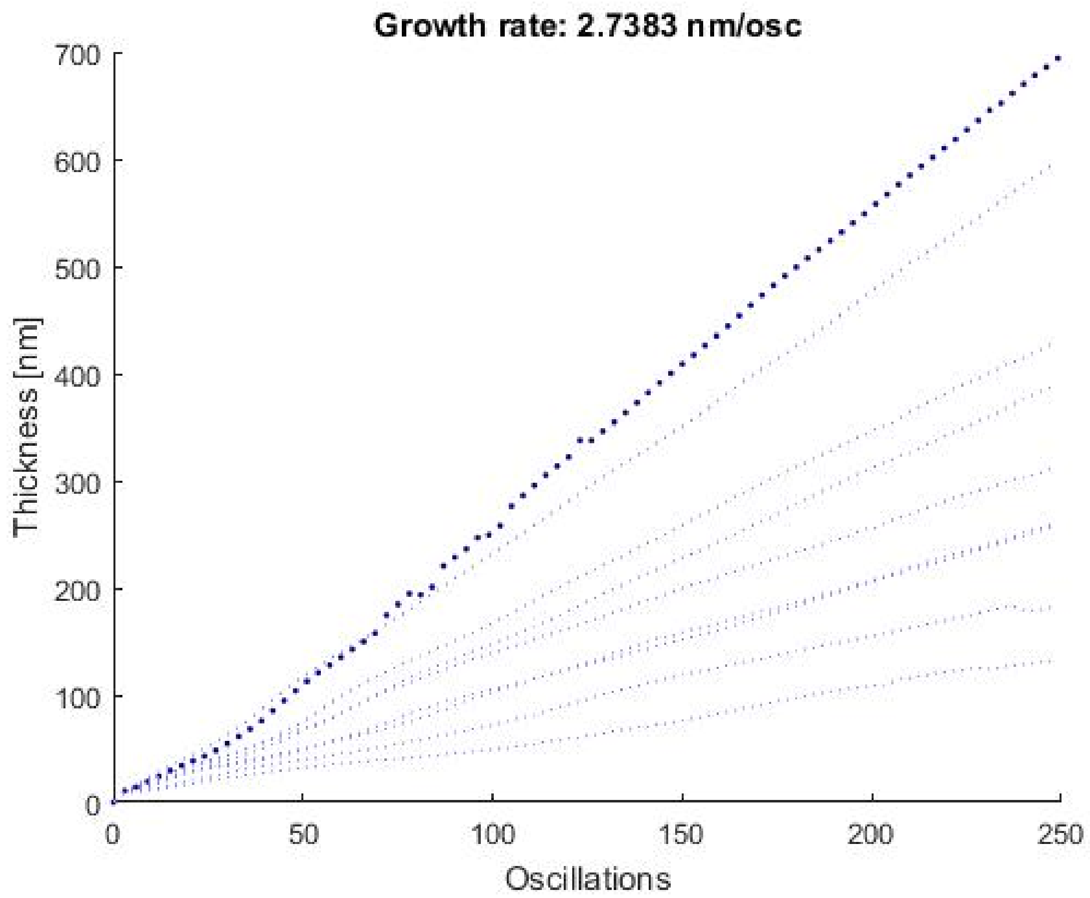

Figure B.2: Thickness as a function of number of oscillations deposited with 100 SCCM of precursor and 125 SCCM of nitrogen curtain

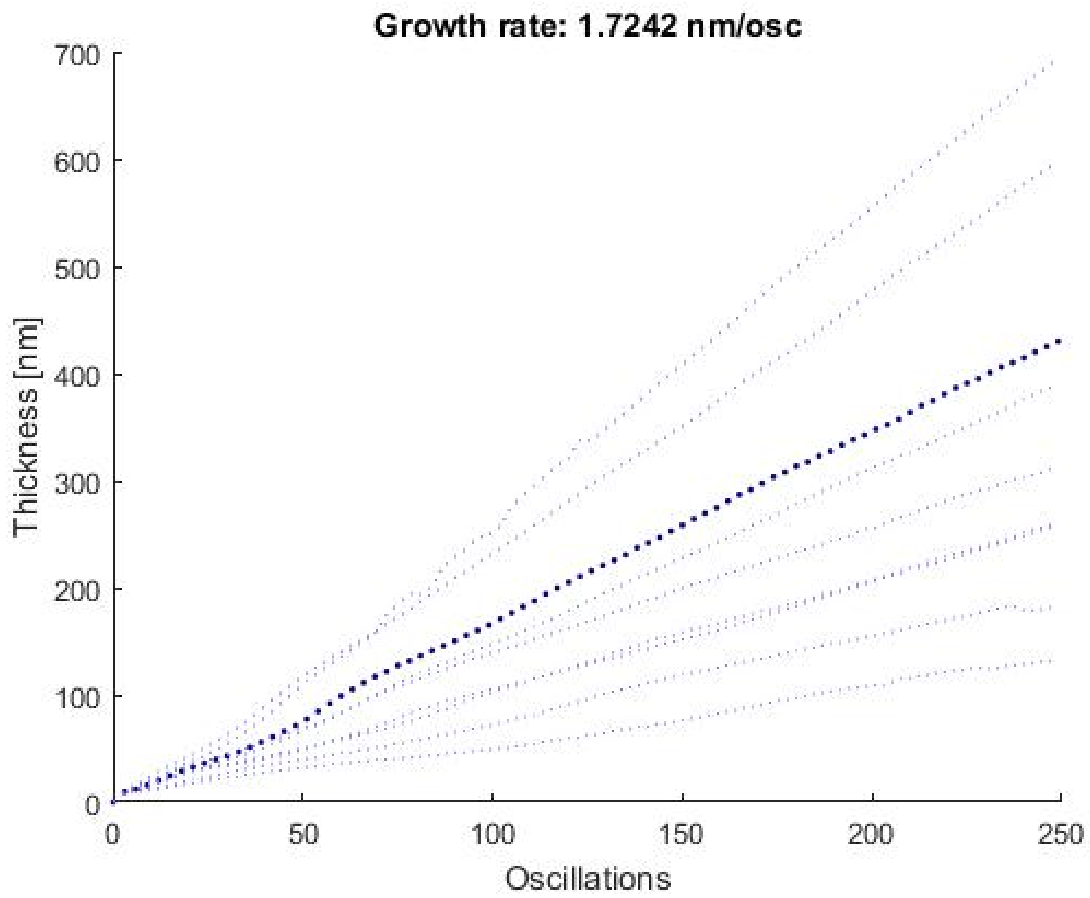

Figure B.3: Thickness as a function of number of oscillations deposited with 150 SCCM of precursor and 125 SCCM of nitrogen curtain

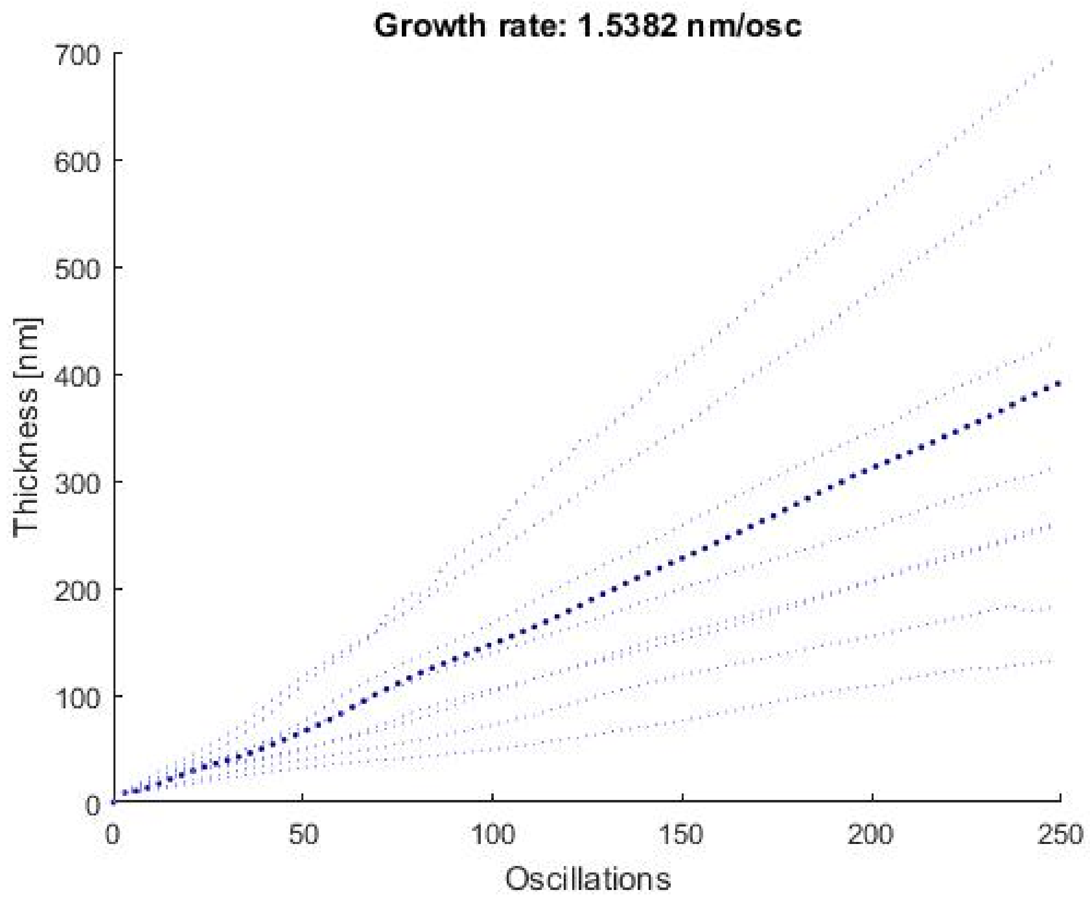

Figure B.4: Thickness as a function of number of oscillations deposited with 50 SCCM of precursor and 208 SCCM of nitrogen curtain

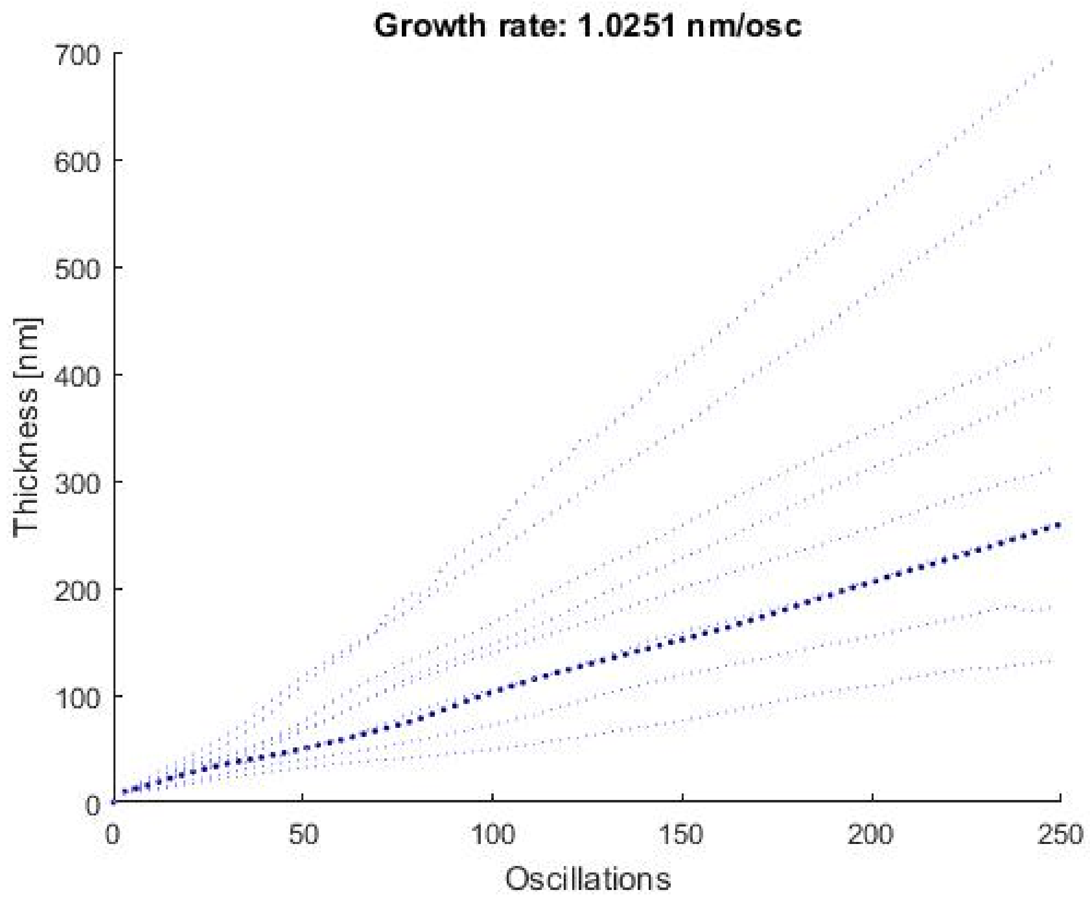

Figure B.5: Thickness as a function of number of oscillations deposited with 100 SCCM of precursor and 208 SCCM of nitrogen curtain

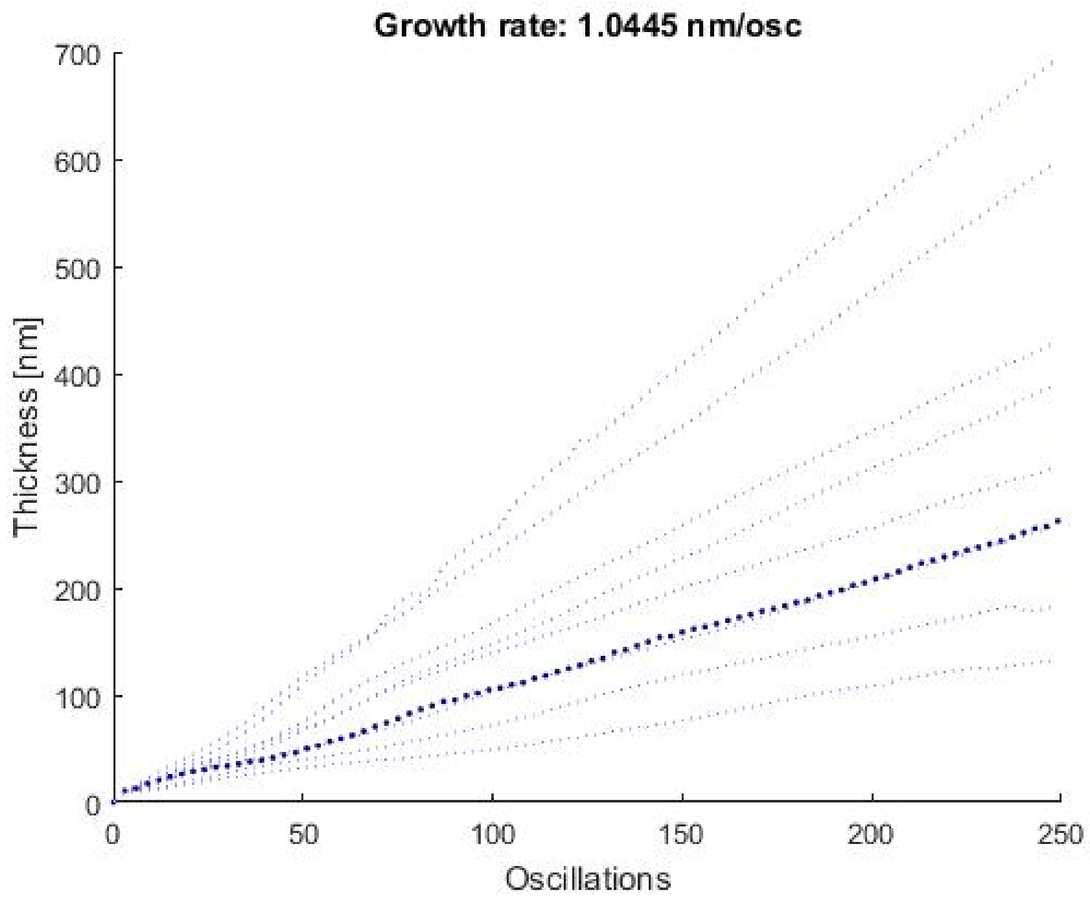

Figure B.6: Thickness as a function of number of oscillations deposited with 150 SCCM of precursor and 208 SCCM of nitrogen curtain

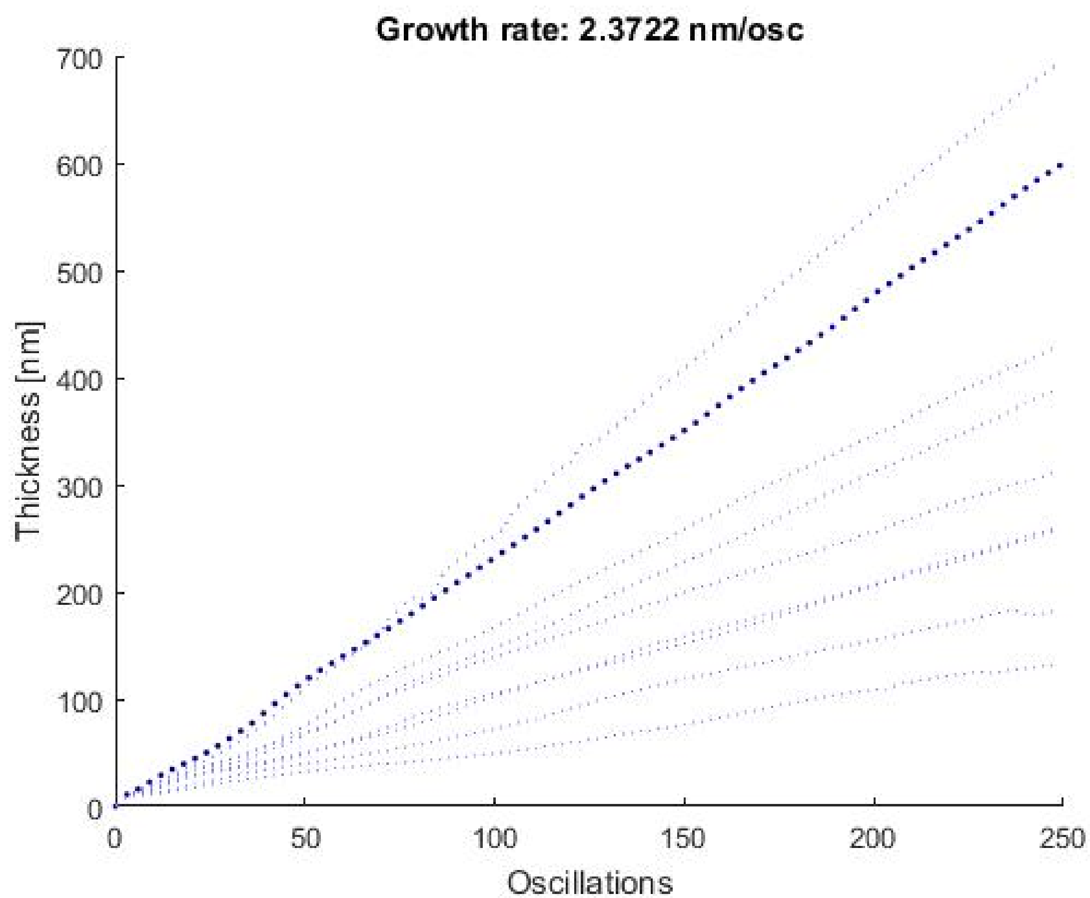

Figure B.7: Thickness as a function of number of oscillations deposited with 50 SCCM of precursor and 333 SCCM of nitrogen curtain

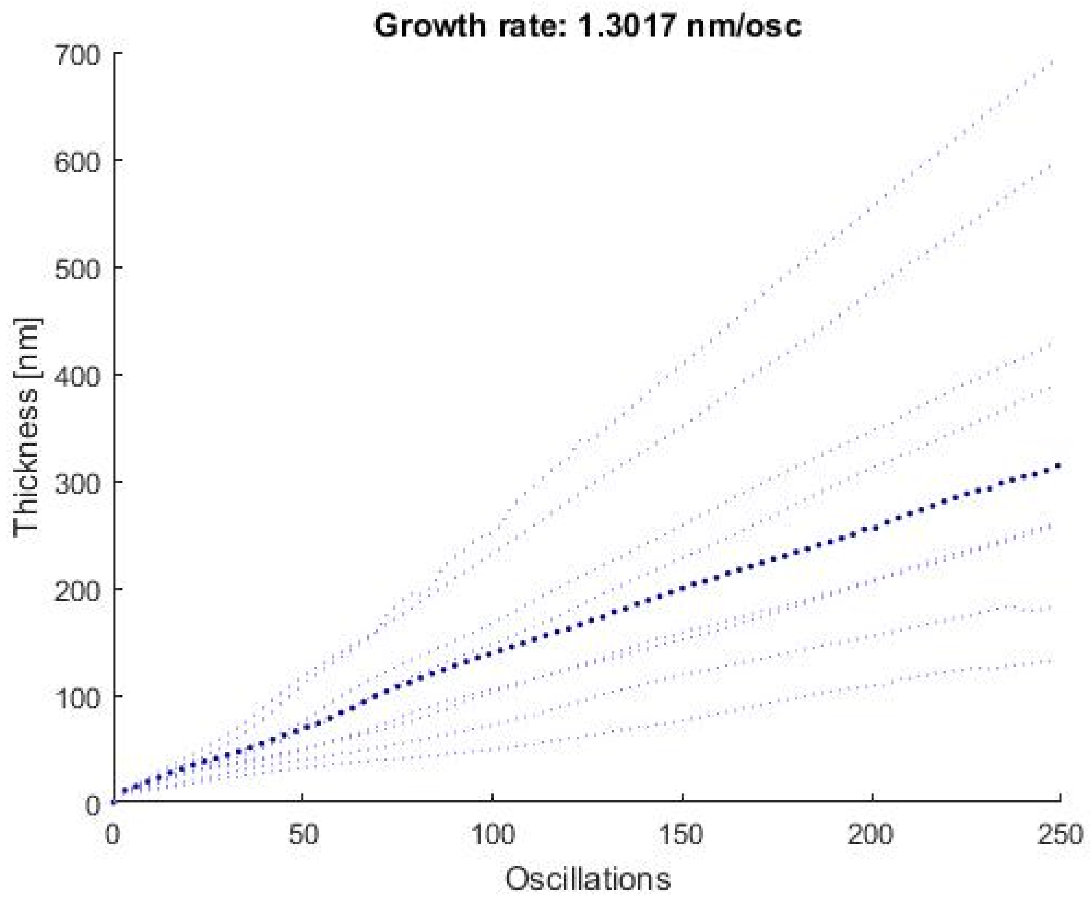

Figure B.8: Thickness as a function of number of oscillations deposited with 100 SCCM of precursor and 333 SCCM of nitrogen curtain

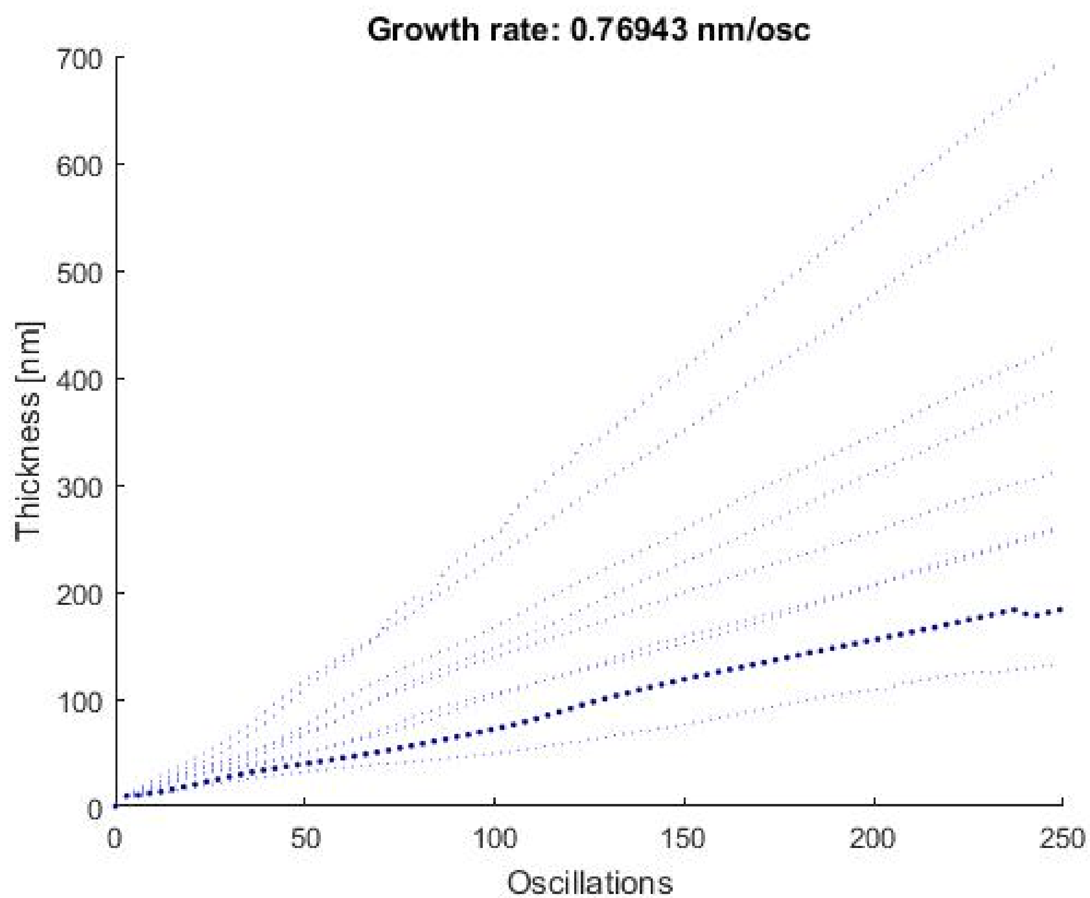

Figure B.9: Thickness as a function of number of oscillations deposited with 150 SCCM of precursor and 333 SCCM of nitrogen curtain

Appendix C

Artificial Neural Network Details

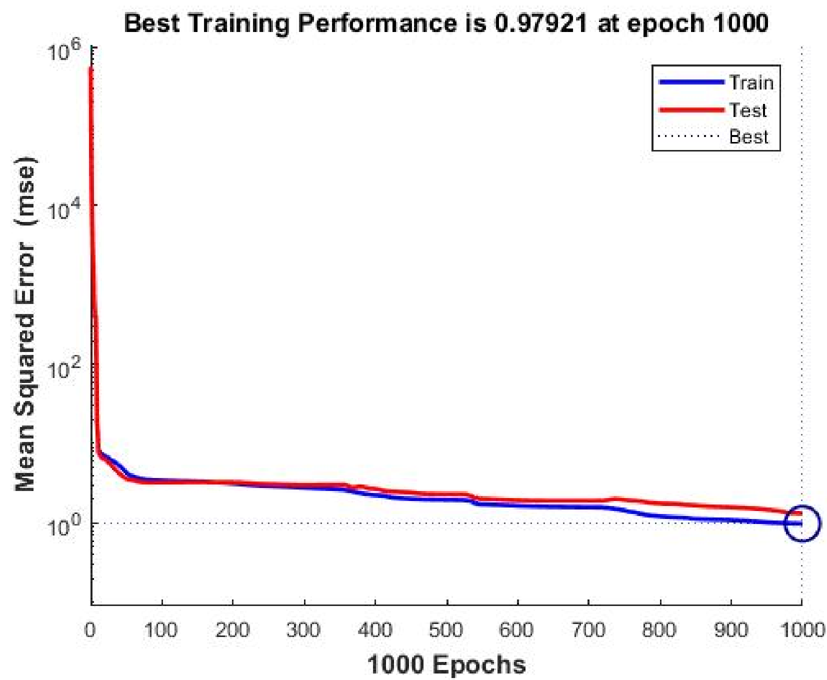

Figure C.1: A plot of the ANN's performance as a function of epochs

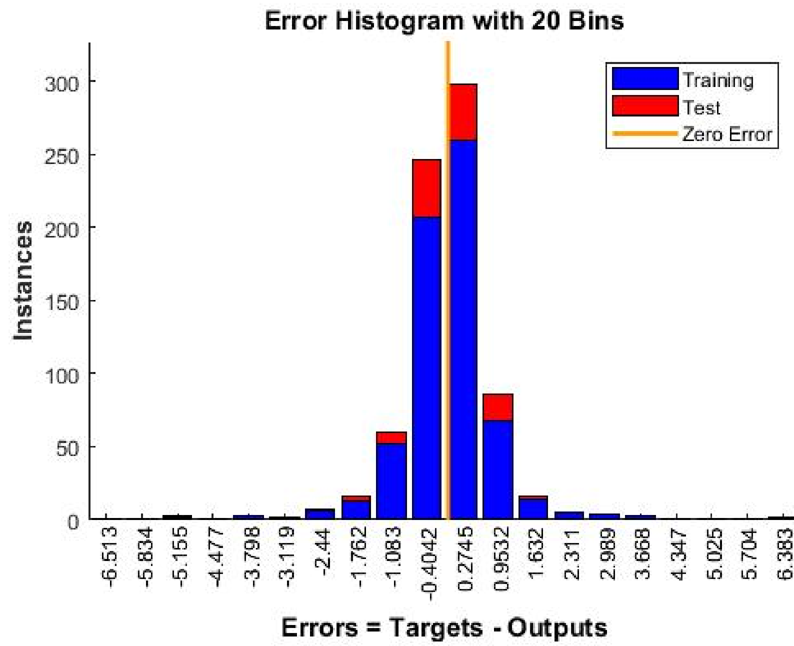

Figure C.2: The error histogram of the ANN where the x-axis is divided into 20 bins. The size of each bin is ∼0.67. The error of each data point is sorted into the corresponding bins. The closer the instances of error are around the zero error line, the better the fit.

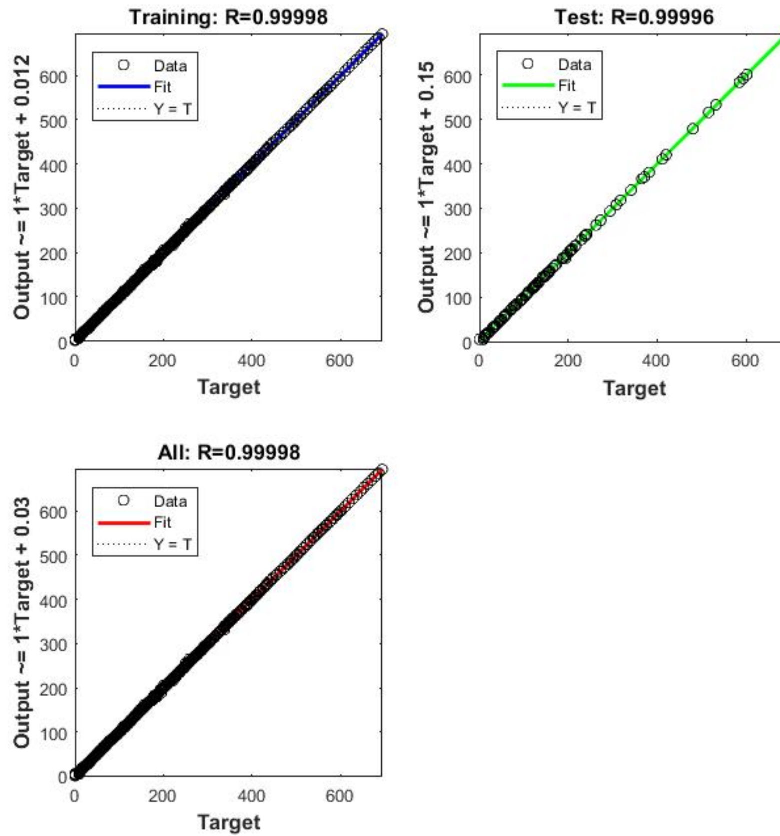

Figure C.3: The regression plot of the ANN where the x-axis is the target value the ANN is trying to predict. The y-axis is the true output of the ANN. A perfect fit will result in all data point on the Y=T line (slope of 1 and y-intercept of 0) and an R-value of 1.